



## Ore genesis and critical metal enrichment using deep learning algorithms in Gunga Pb-Zn deposit, Southern Pakistan: Constraints from sphalerite geochemistry and isotopic compositions

Muhammad A. Gul<sup>a,b</sup>, Huishan Zhang<sup>c,\*</sup>, Yu Yang<sup>a,b,\*\*</sup>, Guangli Ren<sup>c</sup>, Chao Sun<sup>c</sup>, Xiaoqian Zhao<sup>c</sup>, Tahir Bin Yousuf<sup>d</sup>, Ahmed Shah<sup>a,b,e</sup>, Rizwan Sarwar Awan<sup>f</sup>, Mohamed Faisal<sup>g,h</sup>, Xiaoyong Yang<sup>a,b</sup>

<sup>a</sup> CAS Key Laboratory of Crust-Mantle Materials and Environments, University of Science and Technology of China, Hefei 230026, China

<sup>b</sup> CAS Center for Excellence in Comparative Planetology, University of Science and Technology of China, Hefei 230026, China

<sup>c</sup> MNR Key Laboratory for the Study of Focused Magmatism and Giant Ore Deposits, Xi'an Center of Geological Survey, CGS, Xi'an 710054, China

<sup>d</sup> Department of Computer Science and IT, Virtual University, Lahore, Pakistan

<sup>e</sup> Center of Excellence in Mineralogy, University of Baluchistan, Quetta, Pakistan

<sup>f</sup> School of Environment and Resources Engineering, Hefei University of Technology, Hefei, China

<sup>g</sup> Department of Geology, Faculty of Science, Suez Canal University, El-Ismailia 41522, Egypt

<sup>h</sup> School of Geosciences and Info-Physics, Central South University, Changsha 410083, China

### ARTICLE INFO

#### Keywords:

Gunga deposit

Sphalerite geochemistry

Critical metal enrichment

Deep learning algorithms

### ABSTRACT

The Kirthar Fold and Thrust Belt in southern Pakistan is widely recognized as a major metallogenic province owing to the extensive presence of Pb-Zn deposits within the Jurassic sedimentary shelf sequence. One of these deposits, the Gunga Pb-Zn deposit, is a significant economic ore deposit situated within the Anjira Formation and comprises two mineralization zones, the Upper Mineralization Zone (UMZ) and Lower Mineralization Zone (LMZ). Despite the scarcity of documentation on the metallogenic source, origin, mineralization temperature, and other physicochemical conditions, our research is the first to explore the metallogenic differentiation and ore genesis of the deposit by examining minor and trace elements in sphalerite and isotopic analyses (S-Pb). The Gunga Pb-Zn deposit, amounting to 6.86 Mt. with 2.1 % and 11.4 % Pb and Zn, respectively, is linked to the interbedded limestone and shale unit of the Anjira Formation, and approximately below the depth of 200–250 m of the Jurassic-Cretaceous contact, the mineralization is believed to occur in the upper section of the Formation. Sphalerite is the dominant ore mineral, galena is a subordinate mineral, and pyrite is present in the main ore minerals. Sphalerite in the LMZ was found in a vein style, whereas it was disseminated in the UMZ and enriched in (medians) Ge (166 ppm), Cd (541 ppm), Pb (139 ppm), Ag (42 ppm), and Hg (68 ppm), lacking In (0.17 ppm), Co (6 ppm), and Mn (19). Based on trace element concentrations, the LMZ has a reduced environment, higher sulfur fugacity, and higher mineralization temperature (180–200 °C) than the UMZ, which has a lower mineralization temperature (130–180 °C). The presence of black shales, low temperatures, and high sulfur fugacity are the key parameters for Ge enrichment in the Gunga deposit. The  $\delta^{34}\text{S}$  values range from −10 to +5.6 ‰, suggesting that reduced sulfur was produced by both the BSR and TSR mechanisms, with basinal brines and seawater being the main sources of sulfur. The Pb isotope results suggest that the upper crust is the main source of the metals. In this study, Deep Learning algorithms based on sphalerite trace elements were employed for metallogenic discrimination of Pb-Zn deposits. The classifiers were trained on a dataset comprising approximately 3800 data points from 99 mineral deposits with published trace element compositions. The performance of the classifiers was assessed using a cross-validation with a k-fold variant. This study employed well-established classifiers on newly acquired geochemical data obtained from sphalerite samples collected from the Gunga Pb-Zn deposit. Based on the findings of this study, low temperature, lack of magmatic source elements, and

\* Corresponding author.

\*\* Correspondence to: Y. Yang, CAS Key Laboratory of Crust-Mantle Materials and Environments, University of Science and Technology of China, Hefei 230026, China.

E-mail addresses: [zhanghuishan.2086@163.com](mailto:zhanghuishan.2086@163.com) (H. Zhang), [iyangyu@mail.ustc.edu.cn](mailto:iyangyu@mail.ustc.edu.cn) (Y. Yang).

lastic sedimentary sequence in a passive margin environment, a CD-type mineralization is proposed for the Gunga Pb-Zn deposit.

## 1. Introduction

Sediment-hosted Pb-Zn deposits, which are primarily composed of Mississippi Valley-type (MVT) deposits in carbonate-dominated sedimentary rocks and clastic-dominated (CD) deposits in siliciclastic-dominated sequences, represent an important source of Pb and Zn resources, accounting for >80 % (Mudd et al., 2017) of the global

consumption of these metals. These deposits are significant sources of other key metals, including 90 % of the world's cadmium (Cd), 30 % of germanium (Ge) and gallium (Ga) (except for bauxite), and small amounts of indium (In), cobalt (Co), and thallium (Tl) (Mudd et al., 2017; Wen et al., 2020; Li et al., 2023a; Song et al., 2023). The formation of sedimentary rock-hosted Pb-Zn deposits typically involves these key metals as products of Pb and Zn, which are greatly enriched during the

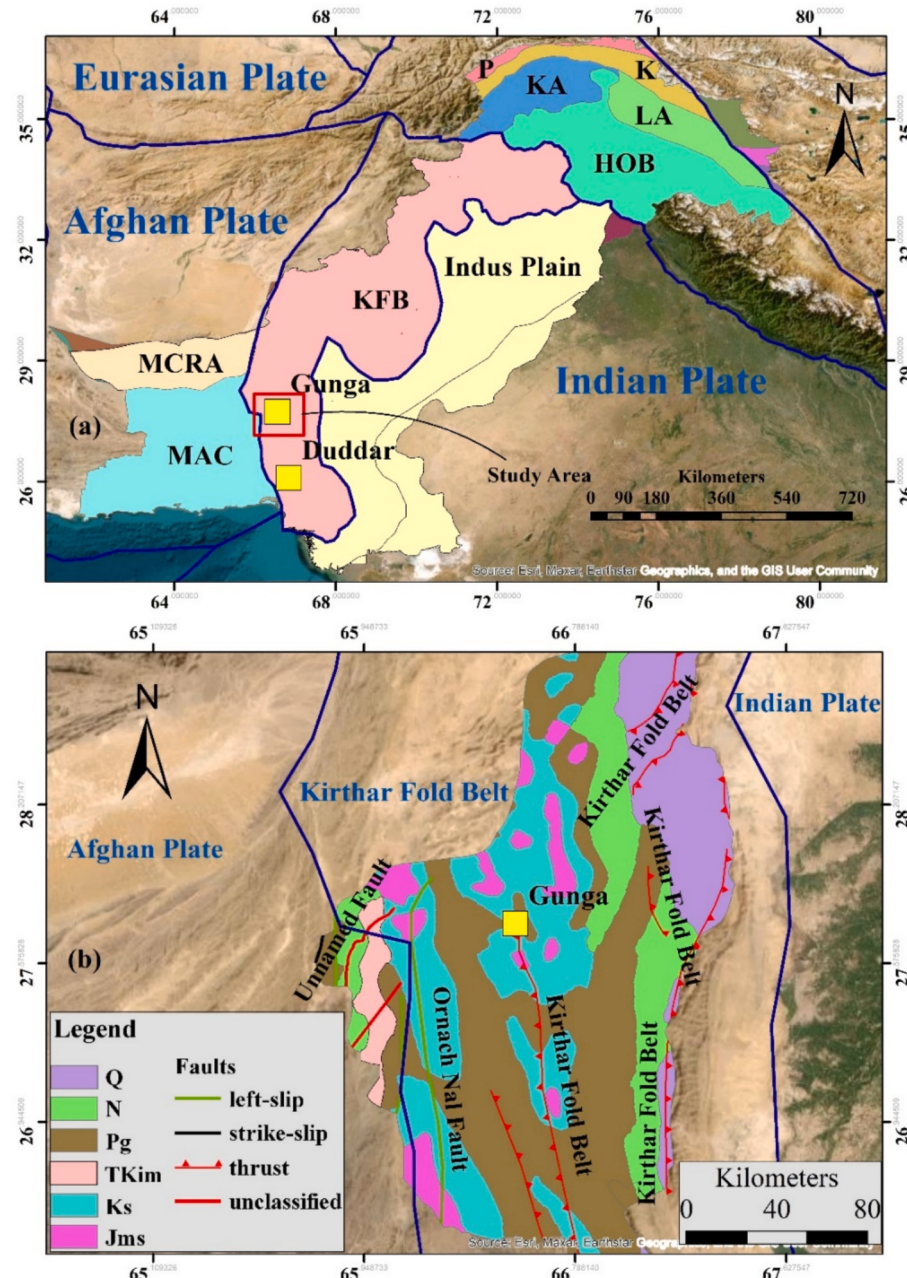


**Fig. 1.** (A) Geological Provinces of Pakistan and locations of Gunga Pb-Zn Deposit. Data for geological Provinces taken from Hasterok et al. (2022). Abbreviations: FTB: Fold and Thrust Belt, HOB: Himalayan Orogenic Belt, K: Karakoram, KA: Kohistan Arc, LA: Ladakh Arc, MAC: Makran Accretionary Complex, MCRA: Makran-Chaghai-Raskoh Arc, P: Pamir, Q: Qiantang. (B) Geology of District Khuzdar. Jms: Jurassic metamorphic and sedimentary rocks, Ks: Cretaceous Sedimentary rocks, TKim: Cretaceous-Tertiary igneous and metamorphic rocks, Pg: Paleogene sedimentary rocks, N: Neogene Sedimentary rocks, Q: Quaternary Sedimentary rocks. The bold blue line shows Tectonic Plate boundaries. The Figure adopted from Gul et al. (2025). (For interpretation of the references to color in this figure legend, the reader is referred to the web version of this article.)

processing and smelting of these metals, making them valuable for recovery (Mudd et al., 2017; Wen et al., 2020; Li et al., 2023a, 2023b; Song et al., 2023).

Sphalerite is frequently found in various ore deposits, including MVT, volcanogenic massive sulfide (VMS), sedimentary exhalative deposits (SEDEX), skarn, metamorphosed sulfide, and epithermal vein systems. The concentrations and arrangement of minor and trace elements in sphalerite are influenced by several factors, including temperature, pressure, pH-Eh conditions, composition of ore fluids, and mineralization and crystallization processes. This information provides insight into the characteristics of the hydrothermal fluids, the onset and progression of ore production, and various types of ore genesis. Research has shown that trace element concentrations in sphalerite can be used to categorize Pb-Zn deposit types. Furthermore, key factors derived from these elements can be utilized in machine learning algorithms to distinguish between different Pb-Zn deposit classifications (Cook et al., 2009; Zhang et al., 2022; Niu et al., 2023; Li et al., 2023a, 2023b; Miao et al., 2023). Machine-learning algorithms have been used to classify deposit types based on the geochemistry of pyrite (Gul et al., 2025), sphalerite, and magnetite. The techniques used included Support Vector Machine (SVM), Random Forest (RF), Extreme Gradient Boosting (XGBoost), Light Gradient-Boosting Machine (lightGBM), cluster analysis and Artificial Neural Network (ANN) (Figueroa and Gregory, 2017; Gregory et al., 2019; Jooshaki et al., 2021; Parsa, 2021; Zhang et al., 2022; Sun et al., 2022a; Sun and Zhou, 2022; Li et al., 2023a; Freij et al., 2023).

Situated along the western edge of the Indian Plate, the Gunga deposit (6.86mt; 11.4 % Zn and 2.1 % Pb) is a component of the Lasbela-Khuzdar metallogenic province. Lead-zinc mineralization is present in the Anjira Formation, which belongs to the Ferozabad Group and dates back to the Early to Middle Jurassic period. The deposit is situated at longitude 66° 32' E and latitude 27° 44' N, approximately 11 km southwest of Khuzdar and 3 km southeast of Gunga Village (Fig. 1). Jancovic (1986) discovered this deposit and described its geology, stratigraphy, and mineralogy. Husain et al. (2002) discussed the genesis of barite deposits using S isotope composition and trace elements, but no study has yet examined the detailed ore genesis for Pb-Zn mineralization. The metallogenic belt for Pb-Zn mineralization is extensive, and at least one-third of it remains to be explored (Zhang et al., 2024). Therefore, it is crucial to enhance our understanding of the mineralogy, temperature, and other physical and chemical factors governing ore mineralization to guide the exploration of new prospects and better comprehend the known ones.

This research mainly focuses on the Pb-Zn mineralization of the Gunga deposit by employing in situ analysis of minor and trace elements in sphalerite, as well as S and Pb isotopic analyses. To create ML-based classifiers that can distinguish sphalerite from SEDEX, MVT, VMS, epithermal, and skarn type Pb-Zn deposits, minor and trace element concentrations of sphalerite from approximately 99 Pb-Zn deposits (3795 points) were compiled from the published literature. The ore-forming history of the Gunga Pb-Zn deposit was revealed using the trained classifiers. These results were then used to analyze metallogenic discrimination and the following important parameters:

- i. Sources of metals and mechanisms of sulfate reduction.
- ii. Mineralization conditions (temperature, sulfur, and oxygen fugacity).
- iii. Ore fluid composition.
- iv. Critical metal enrichment.
- v. Metallogenic origin of the Gunga deposit.

## 2. Regional geology

Two major tectonic events are linked to the geological setting of the Lasbela and Khuzdar districts. The first event, which took place during the late Triassic-Jurassic period, was the breakup of the supercontinent

Gondwana. At that time, the dominant processes were rifting and extensional tectonics, with sedimentation occurring in these settings. The Jurassic Ferozabad Group's upward facies change, deposited on a transgressive continental shelf with a southeastern terrestrial source, suggested a rifting event. This group consists of clastic and carbonate platform shelf and slope environments, which evolved into calm, distal conditions during the Early Cretaceous period (Figs. 2 and 3) (Husain et al., 2002). The second orogenic event caused the separation of the Indo-Pakistan plate from the Turan block. The Indo-Pakistan plate collided with the Afghan and Central Iran-Lut blocks of the Eurasian plate in the west, resulting in the development of a fold belt and the obduction of the Bela-Khuzdar, Muslimgah, Zhob, Waziristan, and Khost Ophiolitic complexes during the Late Cretaceous-Early Tertiary period (Fig. 2) (Ahsan and Qureshi, 1997; Zaigham and Mallick, 2000; Husain et al., 2002).

The Early-Middle Jurassic limestone, mudstone, shale, siltstone, and sandstone of the Ferozabad Group contain mineralization. Pre-Himalayan deformation is responsible for the tight and steeply descending isoclinal folds that define intensive folding. The Spingwar, Loralai, and Anjira are the three units that make up the Ferozabad Group. Although the Early Cretaceous Sember Formation lies at the top of the Ferozabad Group and is highly folded and disconformable in the Lasbela area, it is either completely missing or only partially visible near Khuzdar. The Anjira Formation of interbedded Jurassic limestone and shale of the Ferozabad Group are linked to the Gunga deposit (Fig. 3) (Ahsan and Qureshi, 1997; Song et al., 2019).

## 3. Deposit geology

The mineralized unit, extending over an area of 1500–2000 m in length and 600–1000 m in width, has a thickness of 100–200 m (Fig. 5). It comprises multiple distinguishable members: barren limestone and shale bed, lower mineralization zone (LMZ), barren limestone and shale bed, upper mineralization zone (UMZ), and siliceous sinter above, starting from the bottom and progressing upwards (Fig. 6) (Jancovic, 1986). The descriptions of these units are as follows:

The footwall is composed of interbedded carbonaceous shale and siltstone, with a gradual transition to mineralized siltstone and shale. This transition is marked by occasional patches of pyrite/marcasite and ore minerals such as galena and sphalerite found in the uppermost portion of the footwall rocks. The **lower mineralized zone** (LMZ) is closely linked to a series of hydrothermal and hydrothermally altered sediments, including siliceous sinter, siltstone, and siderite. The Pb-Zn mineralized zone at lower depths consists of irregular veins and lenses that have formed within the brecciated area. While the mineralization primarily follows the layering of the surrounding rocks in a stratiform manner, it occasionally occurs as epigenetic deposits, filling fractures and open spaces (Figs. 4 and 6). The ore deposits primarily consist of >6 % zinc and 1.5 % lead, with certain areas reaching concentrations above 10 %.

Above the lower mineralized zone lies a **barren bed** of interbedded black, dark-gray bituminous fossiliferous argillaceous limestone and shale, with some siltstone. This bed contains disseminated tiny frambooidal and spheroidal pyrite, which are likely syngenetic and associated with bacterial activity, although they are generally devoid of mineralization. The thickness of this bed ranges from 50 to 100 m.

The **upper mineralized zone** (UMZ) is situated above the barren limestone and the shale bed. The footwall is a bed of siliceous sinter mixed with brownish argillaceous material, and dark-brown disseminated bituminous matter is frequently found in the argillite. The UMZ is characterized by an increasing presence of disseminated barite, Fe-Zn, and Pb sulfides. This zone transitions into a transition zone with a thickness of a few meters, which leads to the main mineralization of galena, sphalerite, and marcasite/pyrite. The main mineralization is associated with the barite bed in the central part of the upper mineralized zone. The ore minerals in the lower portion of the barite-bearing

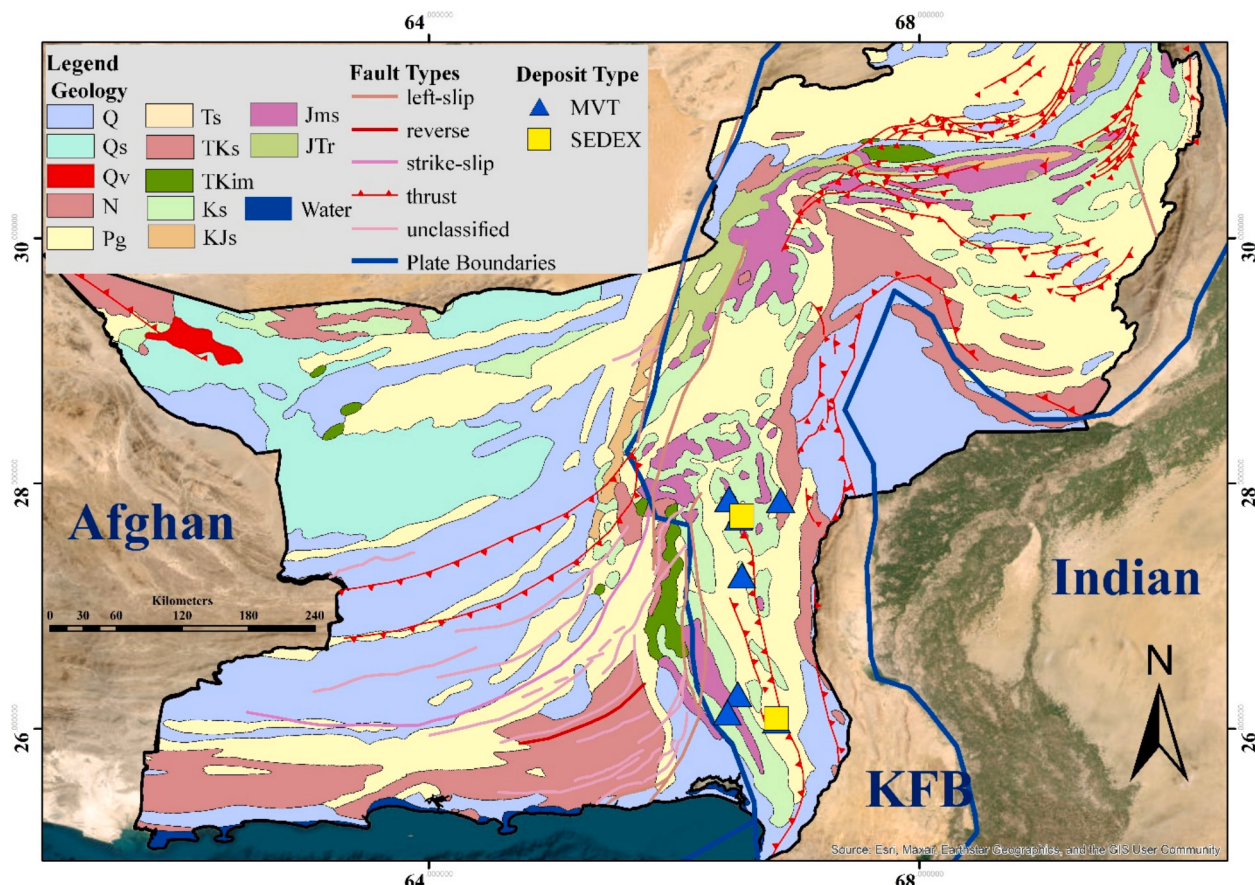


**Fig. 2.** Geological map of Baluchistan Province and Distribution of Pb-Zn Deposits (Hartmann and Moosdorf, 2012). Abbreviations: Q: Quaternary Sediments, Qs: Quaternary Sands, Qv: Quaternary volcanics, N: Neogene Sedimentary rocks, Pg: Paleogene sedimentary rocks, Ts: Tertiary Sedimentary rocks, TKs: Cretaceous-Tertiary sedimentary rocks, TKim: Cretaceous-Tertiary igneous and metamorphic rocks, Ks: Cretaceous Sedimentary rocks, KJs: Cretaceous-Jurassic Sedimentary rocks, JMs: Jurassic metamorphic and sedimentary rocks, Jurasic-Triassic rocks.

zone existed as lenses, patches, and streaks, and there was no sharp transition in the zones containing variable amounts of ore minerals (Figs. 4 and 6). The hanging wall of the mineralized bed was marked by barite mineralization with traces of galena, marcasite, and occasional sphalerite. The uppermost mineralized unit consists of a bed of siliceous sinter, which can be several meters thick, with an abundance of impurities such as limestone and argillite, as well as local barite grains (Jancovic, 1986; Ahsan and Qureshi, 1997).

### 3.1. Ore mineralogy

The mineral associations in the LMZ and UMZ are similar, with the primary difference lying in the concentrations of individual minerals. Mineral paragenesis, including sphalerite, galena, and pyrite as the main ore minerals, is accompanied by traces of chalcopyrite and cinnabar. In the oxidation zone, jarosite, goethite, smithsonite, cerussite, and iron oxides dominate, with traces of native sulfur also present. The major element contents of the ore minerals are presented in Table 1, and the complete mineral paragenesis is illustrated in Fig. 7. Sphalerite serves as the dominant mineral, while galena is the subordinate ore mineral. Sphalerite occurs as vein-like structures in the LMZ and as disseminated mineralization in the UMZ. In contrast, pyrite appears as large crystals and is less hydrothermally altered in the LMZ, whereas in the UMZ, pyrite crystals are small and hydrothermally recrystallized, as indicated by their chemical composition. Fractured galena is observed in the LMZ and is disseminated in the UMZ.

## 4. Sampling and analytical methods

### 4.1. Field and experimental work

More than 120 samples were collected from the Gunga Pb-Zn deposit during two field excursions. These samples were obtained from gossan materials, host rocks, and mineralized zones (Figs. 4 and 6). The samples were then cut and polished to obtain thin sections for microscopic examination. The chosen samples were obtained from both surface and underground mines, and their sulfide mineralogy, textural characteristics, and paragenetic sequences were analyzed. Transmission and reflected light microscopy were used for analysis. Furthermore, representative samples were selected from both zones for in situ and Pb isotope studies, as well as for further analysis using Laser Ablation Inductively Coupled Plasma Mass Spectrometry (LA-ICP-MS) and electron probe microanalysis (EPMA) to identify major, minor, and trace elements. These studies were conducted at the State Key Laboratory of Continental Dynamics, Northwest University, Xi'an, China (in situ S-Pb isotope analysis) and the Xi'an Center of Geological Survey, CGS (EPMA), Xi'an Zhaonian Mineral Testing Technology Co., Ltd., Xi'an, China (LA-ICP-MS). Supplementary Document 1 contains specifications of the analytical techniques.

### 4.2. Deep learning (Neural Networks)

Deep learning, a subset of machine learning, involves training complex artificial neural networks to carry out specific tasks. These networks utilize models with multiple layers, earning the name “deep”

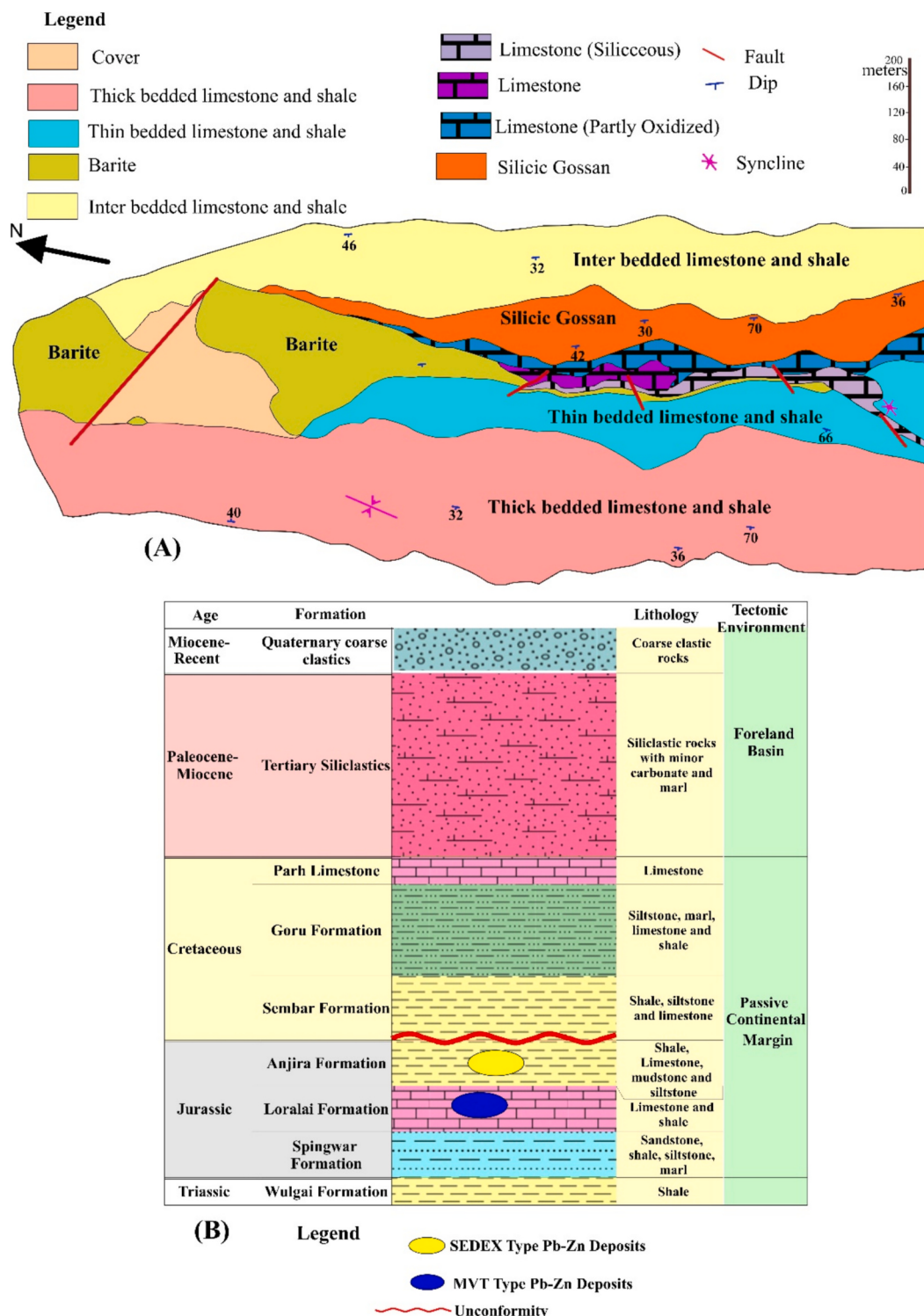


**Fig. 3.** (A) Geological map of Gunga Mine, District Khuzdar, (B) Stratigraphic Column of Lasbela-Khuzdar Region (Ahsan and Qureshi, 1997). The Figure adopted from Gul et al. (2025).

due to their capacity to learn sophisticated hierarchical representations of data. This characteristic makes deep learning particularly effective for applications such as multidimensional data analysis, processing natural language, and recognizing images and audio. The field has shown significant promise in handling extensive and intricate datasets (Sun et al., 2022b; Li et al., 2024; Wang et al., 2024).

We selected this approach based on scalability, transferability, nonlinear relationships, and robustness. Deep learning models are

capable of handling increasing volumes of data, and as datasets grow larger, their performance continues to improve. Additionally, pretrained deep learning models can serve as a solid foundation for new tasks. Deep-learning algorithms can capture intricate and nonlinear patterns in data, and deep-learning models demonstrate resilience when dealing with noisy and unstructured data (Sun et al., 2022b; Li et al., 2024; Wang et al., 2024).

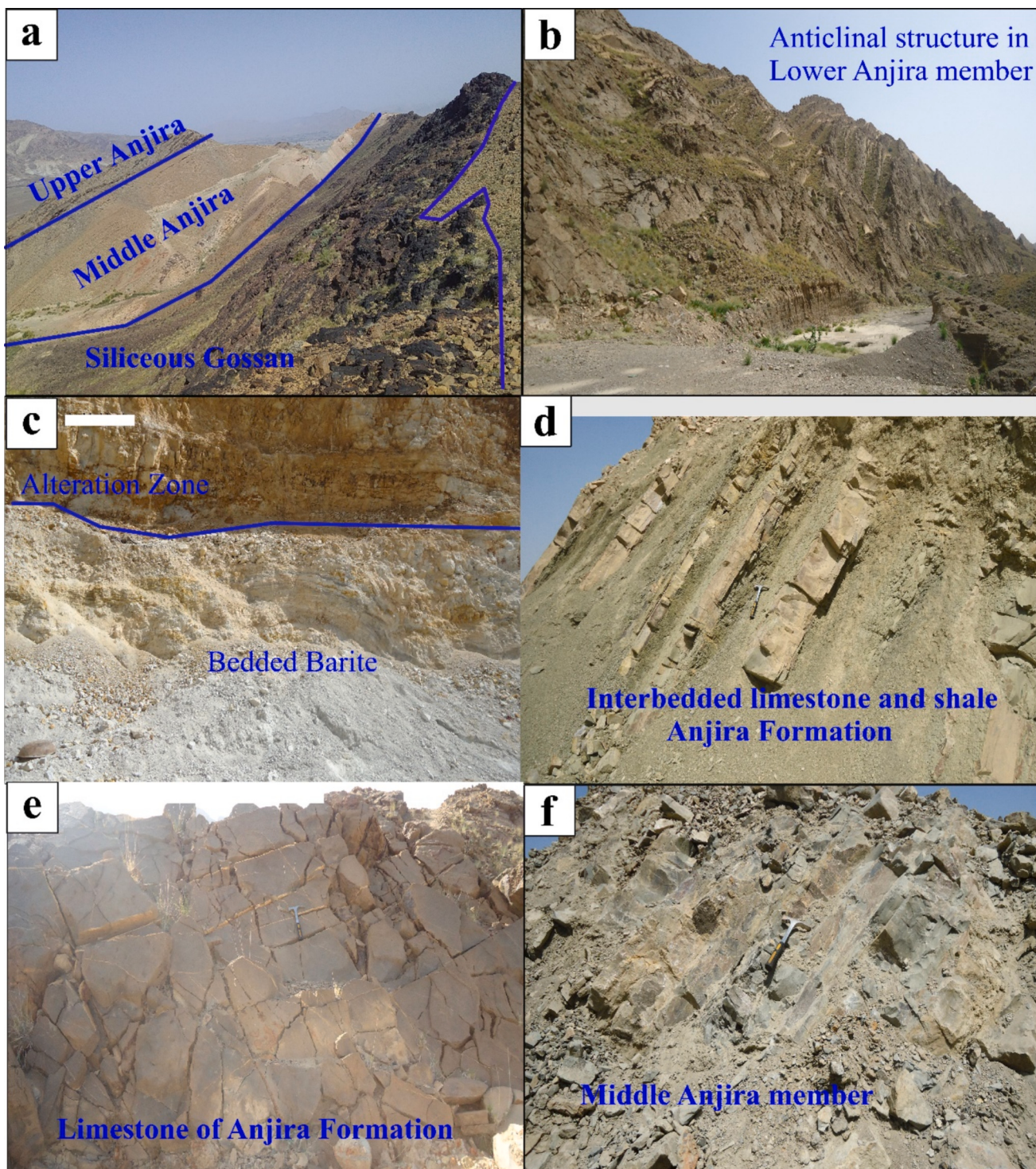


**Fig. 4.** Field photographs of different facies of Anjira Formation (host rock) in Gunga region, District Khuzdar, showing folded structures, bedded facies, contacts between different facies, mineralized gossan, layered barite, and alteration zones. The Figure adopted from [Gul et al. \(2025\)](#).

#### 4.2.1. Data collection and processing

The trace element dataset for sphalerite, comprising 3795 LA-ICP-MS spot analyses of sphalerite compositions, was compiled from 99 lead-zinc deposits (Supplementary Data Table S1). Our study concentrated on five primary Pb-Zn deposit categories: skarn, epithermal, MVT, VMS, and SEDEX. We chose 12 trace elements commonly found in sphalerite due to their frequent analysis and use as element substitutes: Mn, Fe, Co, Cu, Ga, Ge, Ag, Cd, In, Sn, Sb, and Pb. For components that were below detection limits, we employed half of the detection

thresholds in our analysis. Supplementary Data Table S1 provides comprehensive details of the dataset.

Min-Max scaling is used to normalize data for several reasons (Liu and Lin, 2019). First, it is used because features have varying ranges, and it bounds the data within the range of [0,1], treating all features as equally important. Second, Min-Max scaling maintains the relative relationships between the values of a feature. Third, neural networks converge faster when the input features are within a similar scale, and Min-Max scaling helps to achieve this. Finally, while Min-Max scaling is

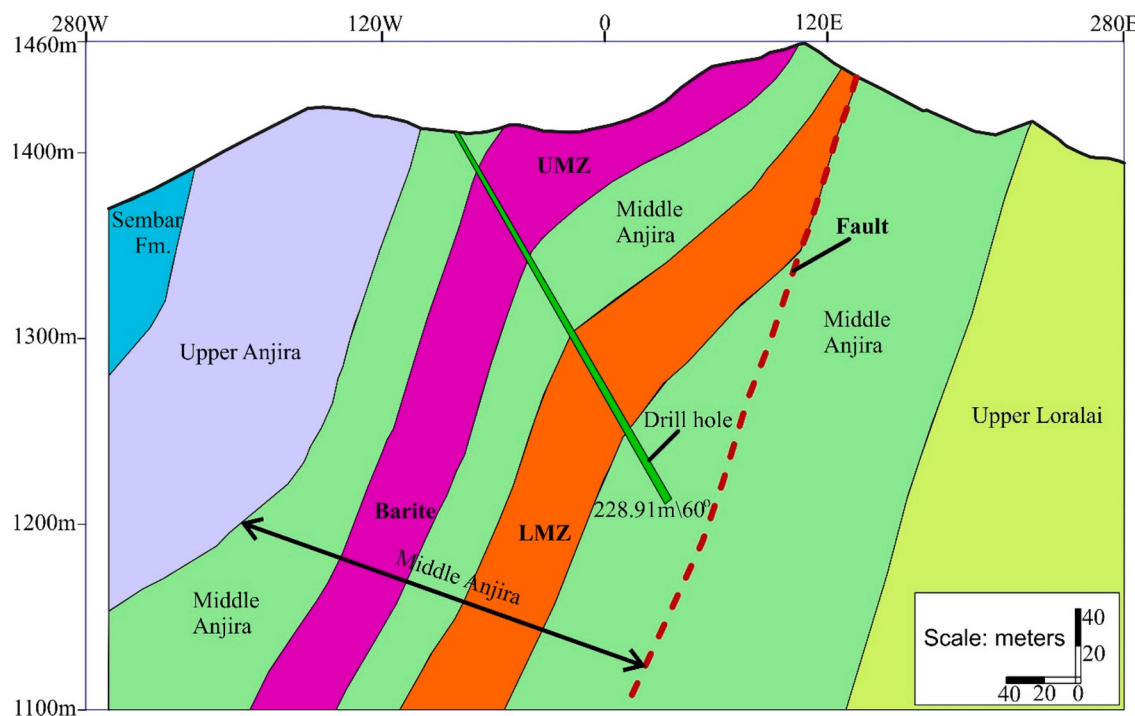


**Fig. 5.** A map of the subsurface structure of the Gunga deposit showing different mineralized zones and the location of the drill hole. It is clear from the map that mineralization is present in the middle Anjira Formation. Abbreviations: LMZ: lower mineralization zone, UMZ: upper mineralization zone. The Figure adopted from Gul et al. (2025).

sensitive to the range of the data, it is less affected by outliers than other scaling methods, ensuring that outliers do not disproportionately influence the scale as they might in other scaling techniques.

$$\text{ForMula Xsc} = (\text{X} - \text{Xmin}) / (\text{Xmax} - \text{Xmin})$$

The distribution of data across all classes was unbalanced. To address this issue, each class was assigned a weight based on its relative representation in the dataset. This approach aims to enhance the performance of the model and to promote more efficient and effective convergence. To address the imbalance issue, class weighting was selected as the preferred approach, as it preserves the original dataset integrity, unlike oversampling or undersampling techniques. Oversampling can potentially lead to overfitting by replicating minority class instances, while undersampling may result in the loss of crucial information from the majority class (Qin et al., 2024). These challenges are particularly significant when the minority class has extremely limited data, as resampling methods might generate artificial examples that fail to accurately represent the minority class's distribution or characteristics. In contrast, class weighting enhances the model's focus on the minority class by adjusting misclassification importance, without risking the introduction of noise or biases that can occur with resampling. This method offers a more sophisticated approach to balancing the model's attention across classes, considering their relative significance without modifying the dataset itself.

The data were divided into training and testing sets, with 20 % allocated for testing and 80 % for training. This division was random to ensure that all classes were represented in both the training and testing sets (Supplementary Data, Table S2).

#### 4.2.2. Model architecture and activation

The selection of neural networks over alternative supervised machine learning approaches, such as Random Forests, was predicated on their capacity to identify intricate, non-linear relationships within geological datasets. The complexity and high dimensionality of interactions among variables in geological data often prove challenging

for conventional methods like Random Forests to model effectively (Ge et al., 2021; Li et al., 2024). Deep learning models, a subset of neural networks, are particularly adept at autonomously learning hierarchical feature representations from raw data through multiple layers of transformation. This enables neural networks to detect subtle patterns and interactions that may not be explicitly defined in the dataset. Furthermore, deep learning enhances generalization by transforming the feature space across successive layers, thereby mitigating the necessity for manual feature extraction. The flexibility and ability to learn directly from large, complex datasets render neural networks more appropriate than Random Forests for tasks where feature interactions are difficult to predetermine, thus justifying their application in this particular context (Ge et al., 2021; Li et al., 2024).

A neural network comprising two hidden layers was implemented using the following specifications: 12 input neurons/features, 400 neurons in the first hidden layer, 200 neurons in the second hidden layer, and five output classes. The number of layers and neurons in each layer was carefully selected and optimized to obtain the best possible results and prevent overfitting and underfitting. The Rectified Linear Unit (ReLU) is frequently employed as an activation function due to several advantages it offers. First, it introduces nonlinearity into the model, which is necessary for neural networks to model complex relationships in the data. Second, the rectification process, which sets the negative values to zero, allows the network to learn nonlinear patterns. Third, unlike activation functions such as the sigmoid and hyperbolic tangent (tanh), ReLU does not saturate for positive values, which helps mitigate the vanishing gradient problem during backpropagation. Finally, ReLU is computationally efficient, making it faster to compute than more complex activation functions such as sigmoid or tanh. This efficiency helps reduce the training time, and the relatively smaller model "dead" neurons are not an issue, making it a suitable choice for many deep learning applications.

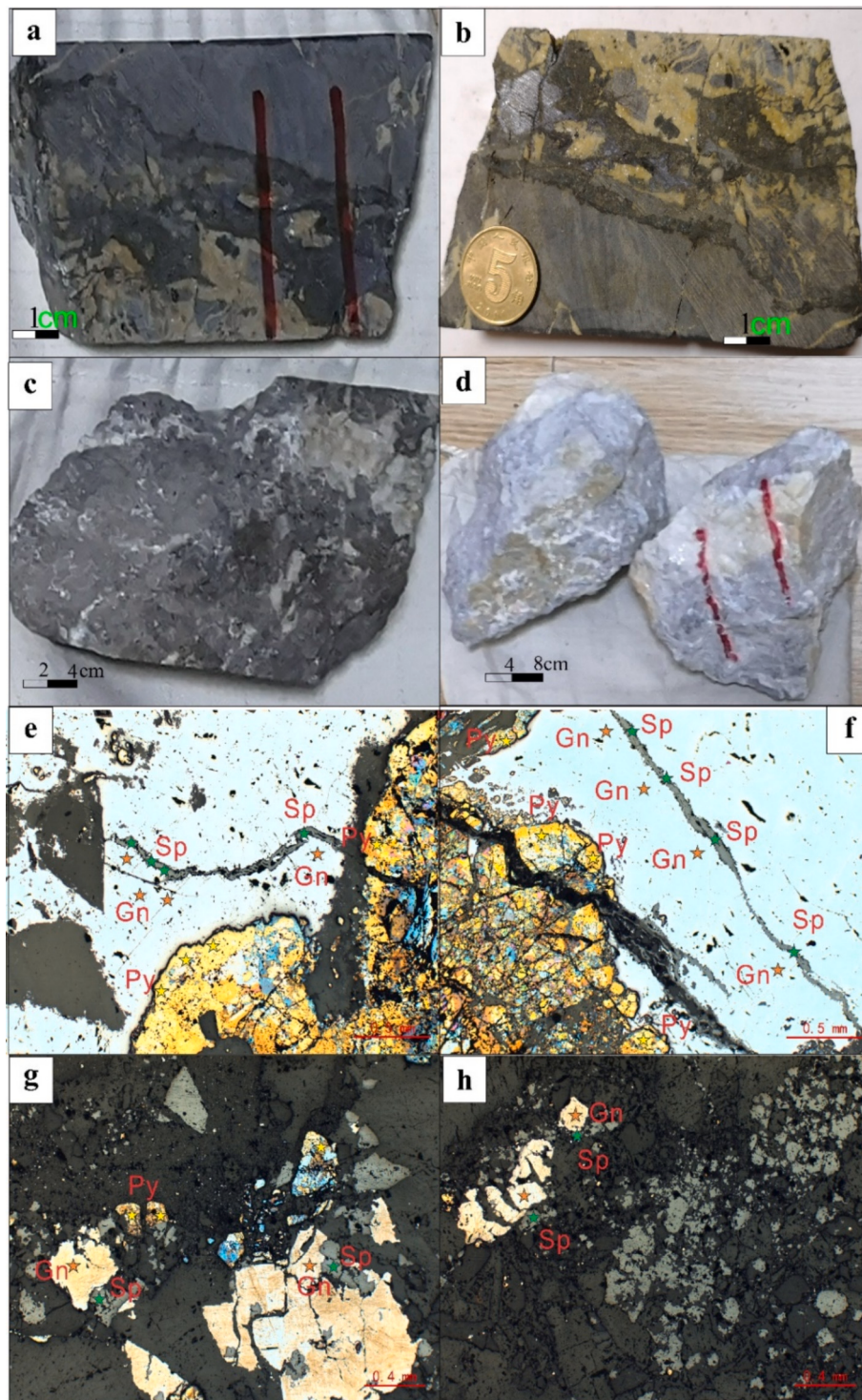


**Fig. 6.** Macroscopic and microscopic characterization of sulfide mineralization from the Gunga Pb-Zn deposit, Southern Pakistan: (a–b) Polished sections of core samples showing sulfide assemblages of sphalerite (gray color), pyrite (light yellow color), and galena (white color); (c) hand specimen with abundant sulfide mineralization from the UMZ; (d) hand specimen of barite from the LMZ; (e–f) reflected light photomicrographs revealing the sulfide mineral assemblages, intergrowth textures, and vein structures from the LMZ; (g–h) photomicrographs of coarse-grained disseminated sulfide minerals from the UMZ. Abbreviations: LMZ: lower mineralization zone, UMZ: upper mineralization zone, Sp: Sphalerite, Gn: Galena, Py: Pyrite. The Figure adopted from Gul et al. (2025). (For interpretation of the references to color in this figure legend, the reader is referred to the web version of this article.)

## 5. Results

### 5.1. Major and trace elements concentration in sphalerite

The sphalerite present in the Gunga deposit has varying levels of Zn,

S, and Fe in the lower mineralized zone (LMZ, sphalerite-I) compared to the upper mineralized zone (UMZ, sphalerite-II). Sphalerite-I has 60 wt % (avg.) Zn, 32.1 (avg.) wt% S, and 4.92 wt% (avg.) of Fe, while 62 wt% (avg.) of Zn, 31.5 (avg.) wt% of S and 2 wt% (avg.) of Fe in sphalerite-II. Although the Fe content was slightly lower than that found in the CD

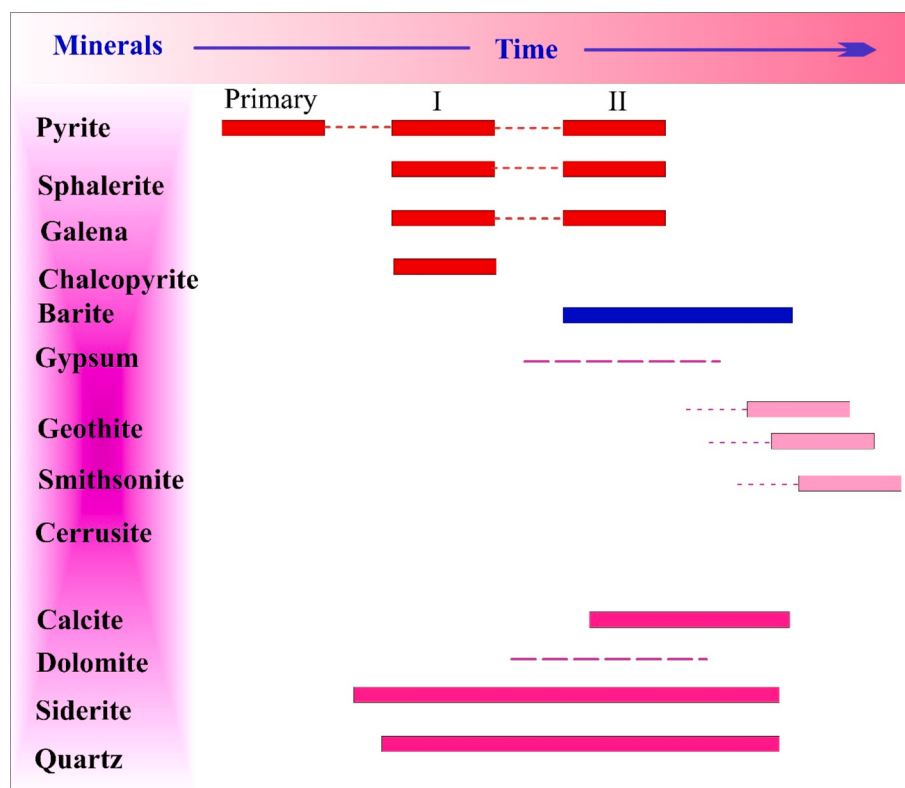


**Fig. 7.** Ore paragenesis of Gunga deposit showing different mineral presence from early to late stages of mineralization. The Figure adopted from [Gul et al. \(2025\)](#).

deposits, as indicated in Fig. 8, it was still significant. It is also worth noting that Fe is more prevalent in sphalerite-I than in sphalerite-II.

The sphalerite samples from the Gunga deposit exhibit diverse trace element concentrations, reflecting their complex geochemical characteristics (Figs. 8 and 9). Table 2 provides a comprehensive summary of the trace elements present in sphalerite from both the lower ( $n = 23$ ) and upper ( $n = 25$ ) mineralized zones of the Gunga Pb-Zn deposits. The sphalerite samples from the Gunga deposit demonstrate distinct trace element distributions between sphalerite-I and sphalerite-II. Cd concentrations range from 246 to 1470 ppm, with sphalerite-I exhibiting higher levels (748.21 ppm) than sphalerite-II (446.35 ppm), significantly lower than values reported for CD deposits. Pb displays substantial variability, ranging from 2 to 23,560 ppm, with sphalerite-II enriched (215.45 ppm) compared to sphalerite-I (132.11 ppm). Cu levels span 2 to 1927 ppm, with sphalerite-I (758.36 ppm) notably more enriched than sphalerite-II (26.26 ppm). Ge concentrations range from 2 to 1014 ppm, with sphalerite-I containing 239.03 ppm compared to 110.15 ppm in sphalerite-II, exceeding typical values for CD deposits. Similarly, Ag concentrations (2–324 ppm) are higher in sphalerite-I (86 ppm) than in sphalerite-II (25.79 ppm), while Sb levels range from 2 to 1216 ppm, with sphalerite-I (136.63 ppm) consistently more enriched than sphalerite-II (25.36 ppm). Sn levels (2–522 ppm) are elevated in sphalerite-I (13.28 ppm) compared to sphalerite-II (3.98 ppm), exceeding the content reported for typical CD deposits. Mn concentrations align with CD deposits (2–1018 ppm), but sphalerite-I (38.33 ppm) contains more Mn than sphalerite-II (9.61 ppm). In concentrations range from 0.07 to 24.87 ppm, with sphalerite-I exhibiting significantly higher levels (0.85 ppm) compared to sphalerite-II (0.04 ppm). Ba exhibits a marked contrast between the upper and lower mineralized zones, with concentrations exceeding 80,000 ppm in the upper zone due to the presence of barite.

The Gunga deposit exhibits a distinct geochemical signature when compared to other deposit types based on median trace element concentrations. It demonstrates enrichment in Ge, Sb, Sn, and Ag, exhibiting

higher median values than most deposit types, particularly SEDEX, VMS, and MVT deposits. Conversely, the median values for In, Cu, Pb, and Mn are generally lower than those observed in VMS deposits, suggesting a less pronounced contribution from metallogenic processes typically associated with these deposits. The variability in element distribution underscores the distinctive nature of the Gunga deposit, differentiating it from magmatic deposits while aligning closely with certain characteristics of sediment-hosted deposits.

### 5.2. LA-ICP-MS profiles of sphalerite

Time-resolved LA-ICP-MS depth profiles are plotted in the current study to elucidate the trace element distribution in sphalerite-I and sphalerite-II. Representative profiles are presented in Fig. 10. The ablation profiles of certain elements (Zn, Fe, Cd, Sn, Ge; Fig. 10D) exhibit smooth patterns without significant fluctuations, indicating that their concentrations are uniformly distributed at the scale of the analyzed spots. Conversely, some elements (In, Ni, Co) display sawtooth ablation profiles due to their low concentrations. Notably, at specific points, ablation profiles with anomalous spikes are observed for the elements Pb, Ge, Mn, and Sn, suggesting the presence of micro- or nanoscale mineral inclusions composed of these elements (Fougerouse et al., 2023; Huston and Bastrakov, 2024).

### 5.3. Sulfur isotope compositions

The results of in-situ isotope analysis for sphalerite and barite from both zones of the Gunga deposit are displayed in Table 3 and Fig. 11. Sphalerite-I exhibited  $\delta^{34}\text{S}_{\text{CDT}}$  values ranging from  $-10.49$  to  $-0.74$  ‰, with a mean of  $-3.88$  ‰ ( $n = 10$ ). In comparison, sphalerite-II showed  $\delta^{34}\text{S}_{\text{CDT}}$  values between  $3.03$  and  $5.64$  ‰ ( $n = 12$ ), averaging  $3.93$ . Barite samples from the UMZ demonstrated  $\delta^{34}\text{S}_{\text{CDT}}$  values spanning from  $18.7$  to  $47.8$  ‰ ( $n = 16$ ), with an average of  $34.14$  ‰.

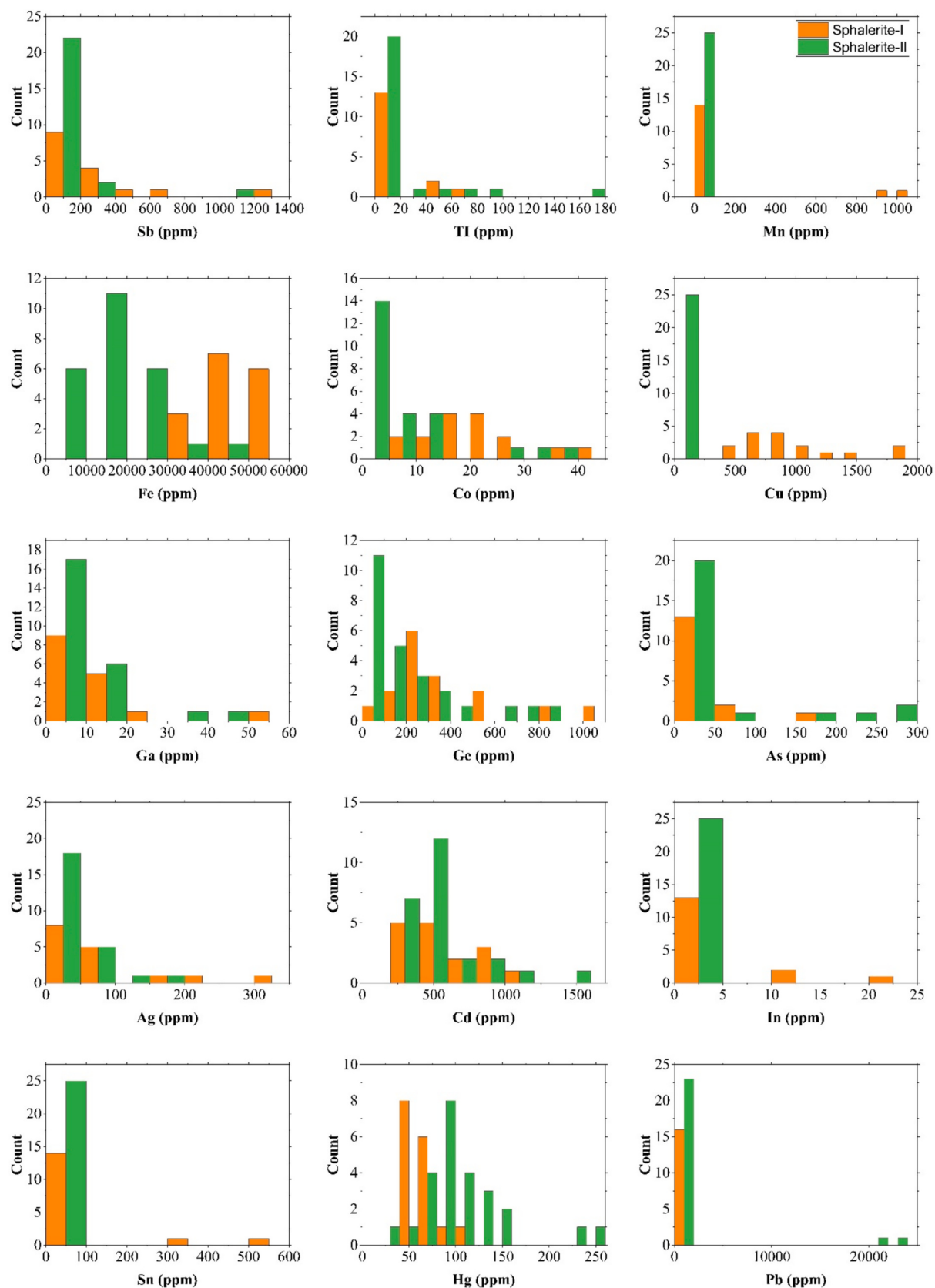
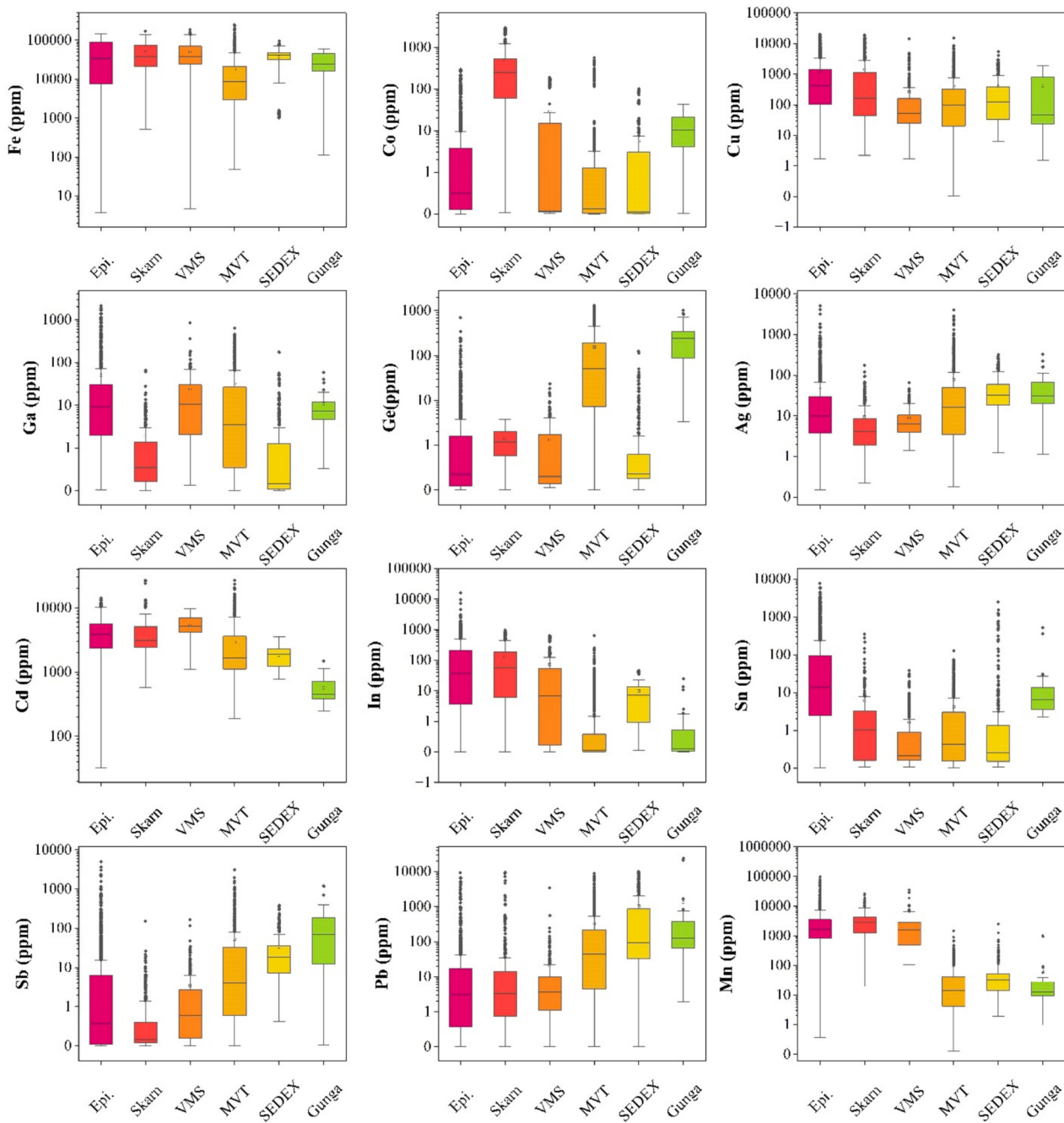


Fig. 8. Histograms of minor and trace elements in sphalerite of both the Upper and Lower mineralization zones from the Gunga Pb-Zn deposit.



**Fig. 9.** Box plots of trace elements of Gunga Pb-Zn deposit and their comparison with global data of all types of Pb-Zn deposits such as SEDEX, MVT, VMS, Skarn and Epithermal (Cook et al., 2009; Li et al., 2023a, 2023b; Ye et al., 2011; Zhang et al., 2022).

#### 5.4. Lead isotope compositions

Table 4 displays the results of the in-situ lead isotope analysis conducted on sphalerite samples from both mineralized zones within the Gunga deposit. The  $^{206}\text{Pb}/^{204}\text{Pb}$  ratios of the analyzed sphalerite range from 18.45 to 18.573, the  $^{207}\text{Pb}/^{204}\text{Pb}$  ratios range from 15.61 to 15.709, and the  $^{208}\text{Pb}/^{204}\text{Pb}$  ratios range from 38.53 to 38.743. The Pb isotope evolution diagram displays these plotted values as presented by Zartman and Doe (1981) in Fig. 12.

#### 5.5. Deep learning (Neural Networks)

The performance of the Neural Network model on the scaled dataset demonstrates robust classification capabilities, achieving an overall

accuracy of 94.73 %. The classification report (Table 5) illustrates strong metrics across all five classes, with precision, recall, and F1-scores consistently high. Class 1 (MVT) exhibited the highest F1-score (0.97), indicating exceptional performance, while Class 3 (Skarn) showed slightly lower precision (0.85) but maintained a satisfactory F1-score (0.90). The macro-average F1-score of 0.94 indicates balanced performance across all classes, while the weighted-average F1-score of 0.95 confirms the model's efficacy in handling class imbalance. Notably, the model performed well for both majority classes, such as Class 0 (Epithermal), and minority classes, such as Class 2 (SEDEX/CD), demonstrating its reliability and generalization capacity. These results underscore the model's effectiveness and suitability for addressing the given multi-class classification problem.

A comparison of the original and predicted deposit types based on

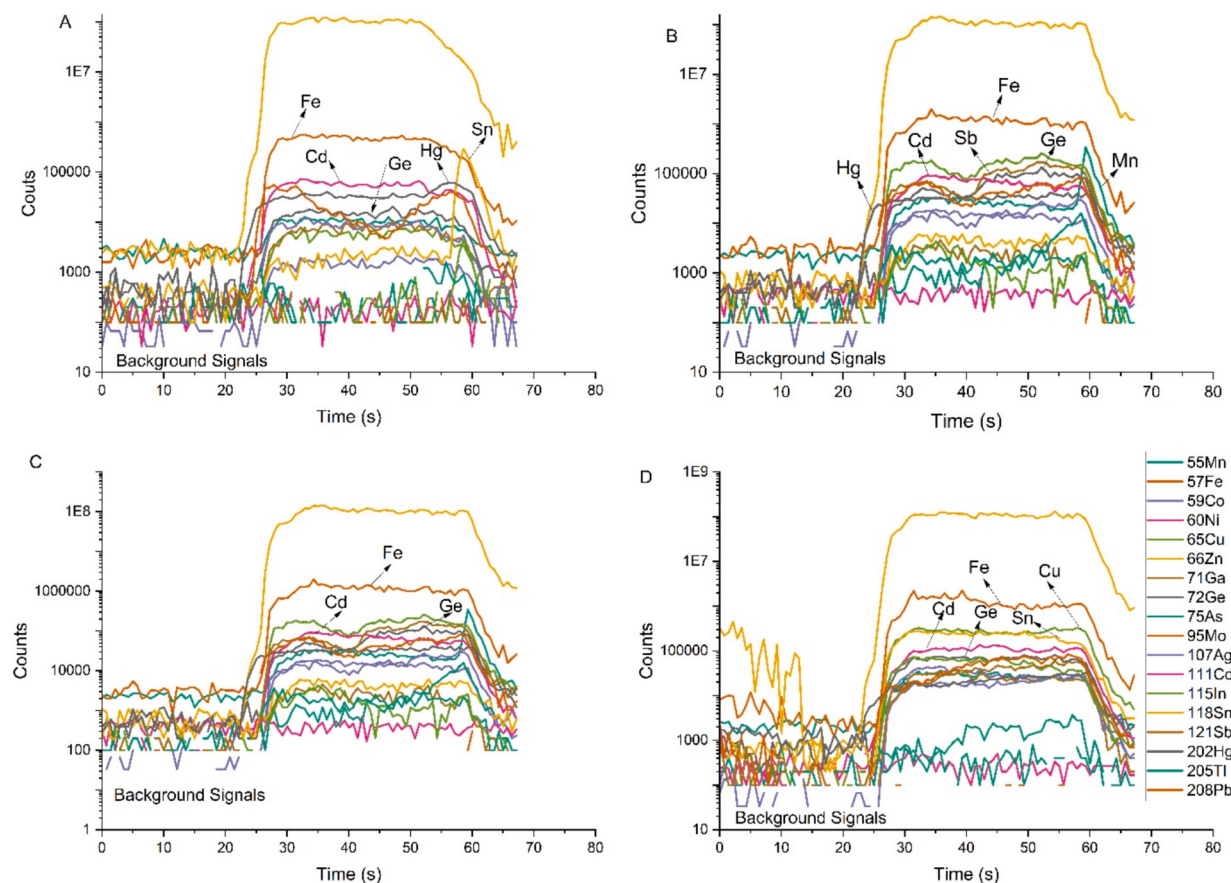


**Fig. 10.** Characteristic LA-ICP-MS depth profiles over time for two sphalerite varieties observed in the Gunga deposit. (A and C) Representative depth profile illustrating sphalerite-I; (B and D) Representative depth profile demonstrating sphalerite-II.

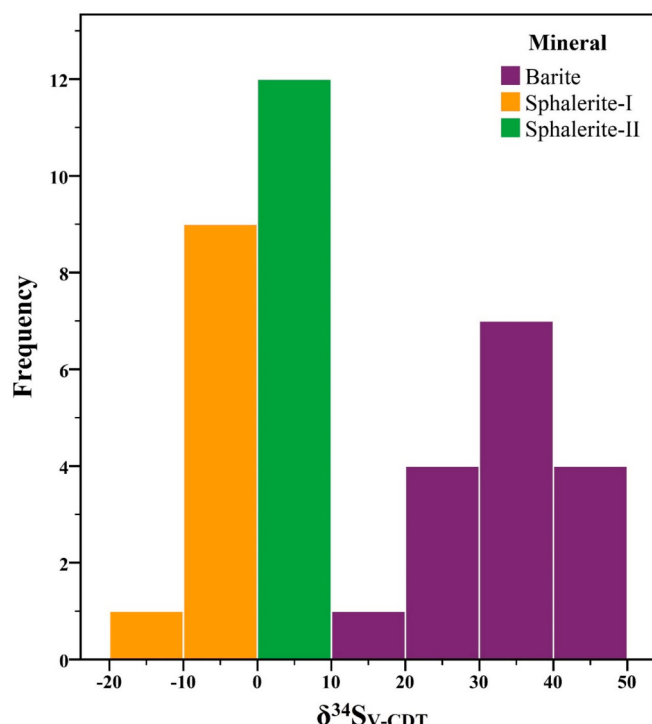


**Fig. 11.** S isotope compositions in Sphalerite and Barite from Gunga Pb-Zn deposit.

the blind test is presented in Fig. 13, which aligns with the aforementioned accuracy. The correspondence between the predicted (green bars) and original (orange bars) values demonstrates the model's performance. Predictions for Epithermal deposits exhibit minimal deviation, indicating the model's accuracy in identifying this category. However, slight over-predictions are observed for MVT and VMS deposits, suggesting some degree of misclassification or overlap in geochemical characteristics. Predictions for Skarn deposits also show close alignment but demonstrate marginal underestimation. Overall, the visualization illustrates the model's robust performance across deposit types, with only minor discrepancies, reflecting its efficacy in classifying mineral deposits.

The trace element concentrations of sphalerite in the Gunga deposit were uploaded in the deep-learning designed model, and the results predicted a CD-type deposit, which is also consistent with geological and geochemical features, such as no magmatic activity near the deposit, higher concentrations of Cd and Ge, and lower concentrations of Ga and In (Zhang et al., 2022; Li et al., 2023a).

## 6. Discussion

The findings of this study indicate that the trace element properties of sphalerite can effectively capture its formation environment and be accurately interpreted through the application of deep learning techniques. Supervised machine learning offers a potent means for interpreting complex geochemical data in multiple dimensions.

### 6.1. Substitution mechanism

Sulfophile elements included Ga, Ge, Ag, Cd, In, Tl, and Pb. Fe and

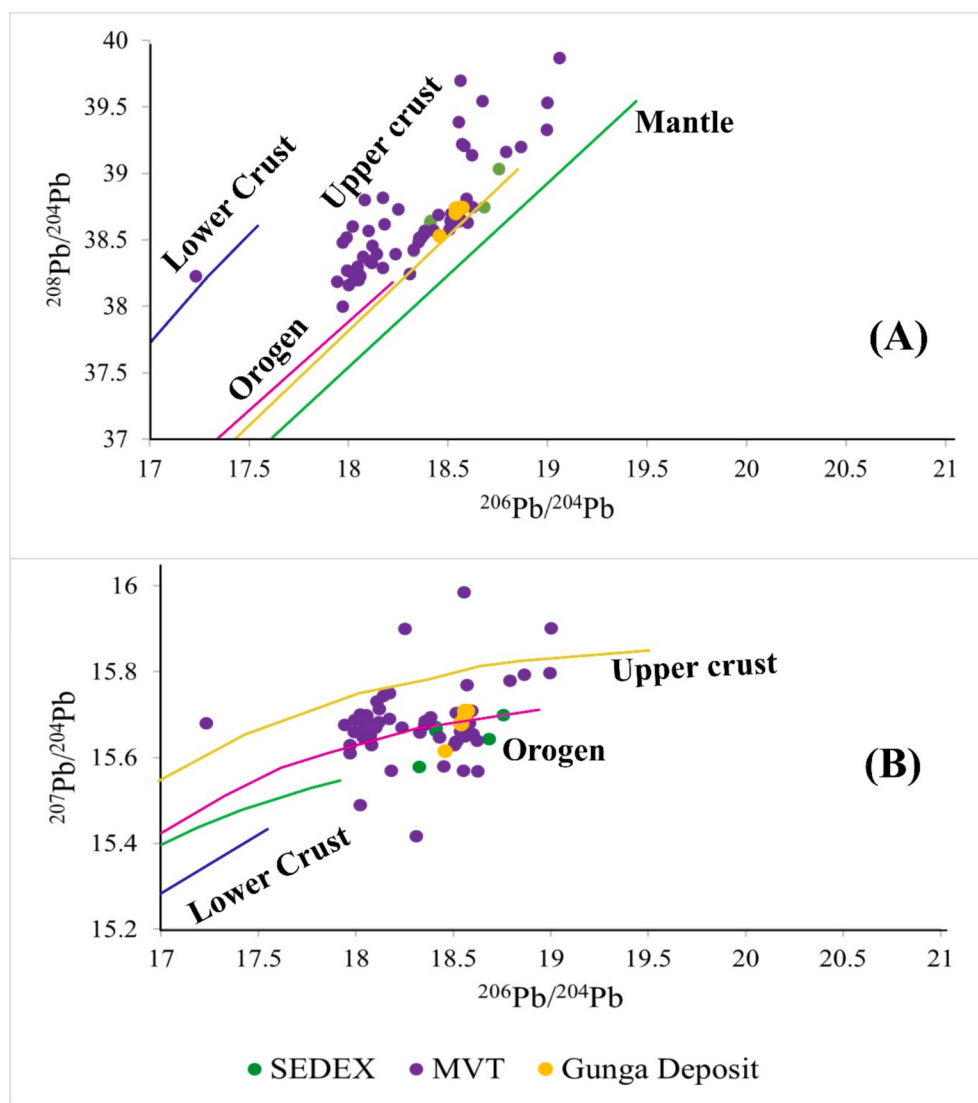


**Fig. 12.** Pb isotope compositions in sphalerite from the Gunga Pb-Zn deposit compared with Pb-Zn deposits of Central Tethyan Domain.

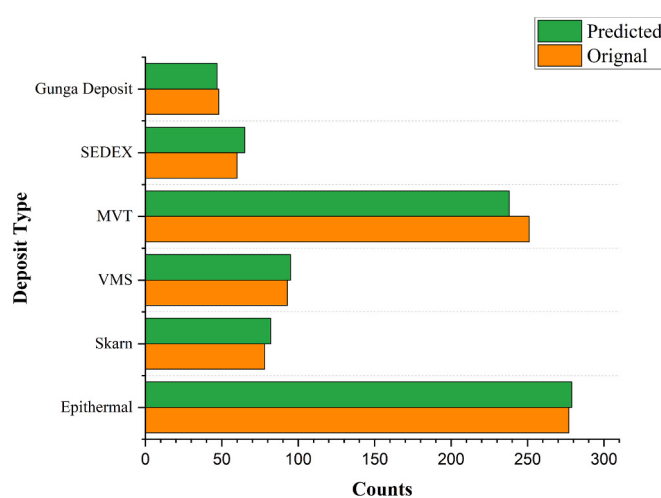


**Fig. 13.** Comparison of original and predicted deposit types based on results of Neural Network model.

Mn easily combine with S to form sulfides. Most of these ions have similar radii and electrovalences. Zn may be displaced into the sphalerite lattice by ions with radii between 104 pm and 44 pm, and isomorphism requires similar electronegativity and polarization. Since  $\text{Fe}^{2+}$ 's ionic radius is closest to that of  $\text{Zn}^{2+}$ , it has the greatest capacity to replace  $\text{Zn}^{2+}$ . Researchers have suggested two primary types of isomorphism (Cook et al., 2009; Lai et al., 2023).

In the first category,  $\text{Zn}^{2+}$  is substituted by ions alone, such as  $\text{Zn}^{2+} \leftrightarrow \text{M}^{2+}$  ( $\text{Fe}^{2+}$ ,  $\text{Mn}^{2+}$ , and  $\text{Cd}^{2+}$ ). In the second category,  $\text{Zn}^{2+}$  is coupled with two or more ions:  $2\text{Zn}^{2+} \leftrightarrow \text{Ag}^+(\text{Cu}^+) + \text{M}^{3+}$ ,  $3\text{Zn}^{2+} \leftrightarrow 2\text{Ag}^+(\text{Cu}^+) + \text{M}^{4+}$ , and  $4\text{Zn}^{2+} \leftrightarrow 2\text{Ag}^+(\text{Cu}^+) + \text{M}^{2+} + \text{M}^{4+}$ . In addition, there are some substitution mechanisms involving lattice vacancies, such as  $3\text{Zn}^{2+} \leftrightarrow \text{In}^{3+} + \text{Sn}^{3+} + \square$ ,  $4\text{Zn}^{2+} \leftrightarrow 2\text{Fe}^{2+} + \text{Ge}^{4+} + \square$ , and  $2\text{Zn}^{2+} \leftrightarrow \text{Ge}^{4+} + \square$  (Lai et al., 2023; Zhao et al., 2023). The inter-element correlation coefficients of the chosen elements are shown in Fig. 14 to clarify the substitution process of these elements. The following substitution process was developed based on these findings and the chemical possibilities.

#### 6.1.1. Sphalerite-I (LMZ)

Multiple studies have revealed that  $\text{Zn}^{2+}$  is often replaced by other divalent cations, including  $\text{Fe}^{2+}$ ,  $\text{Cd}^{2+}$ ,  $\text{Mn}^{2+}$ , and  $\text{Co}^{2+}$  in sphalerite (Cook et al., 2009; Zhang et al., 2022; Li et al., 2023a). Our findings for

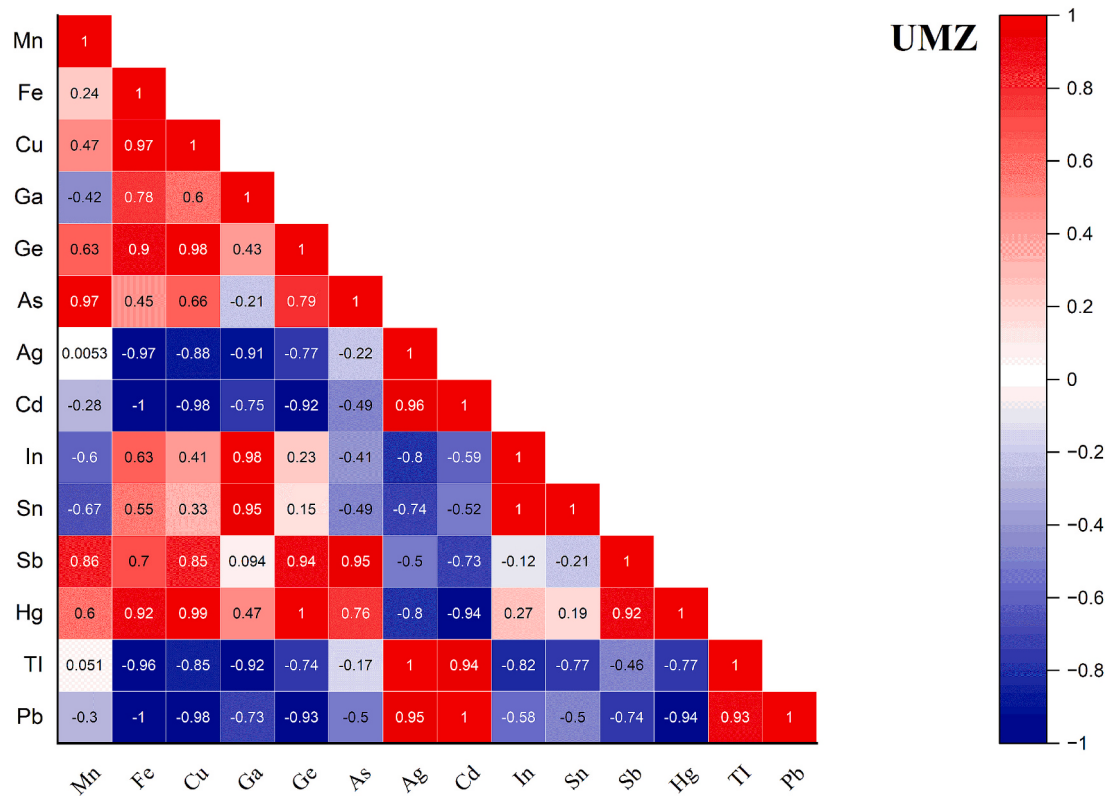
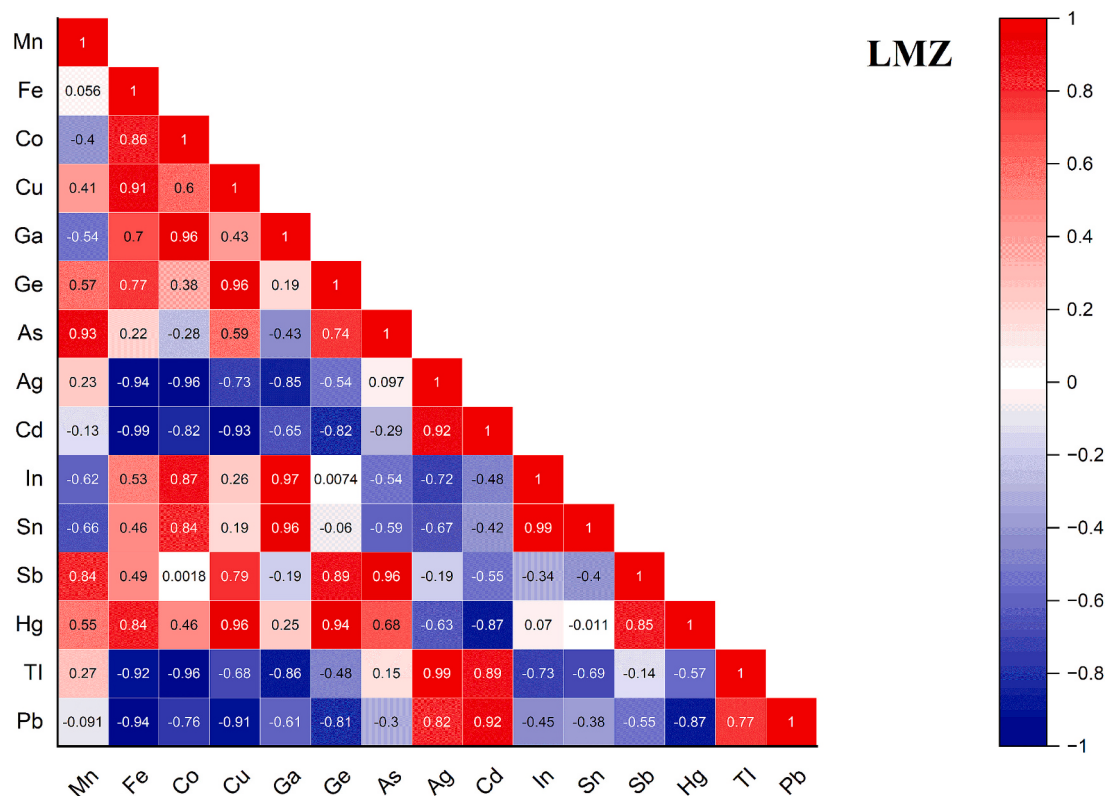


**Fig. 14.** Interelement co-relations of molar ratios of minor and trace elements from LMZ and UMZ based on Pearson correlation coefficient.

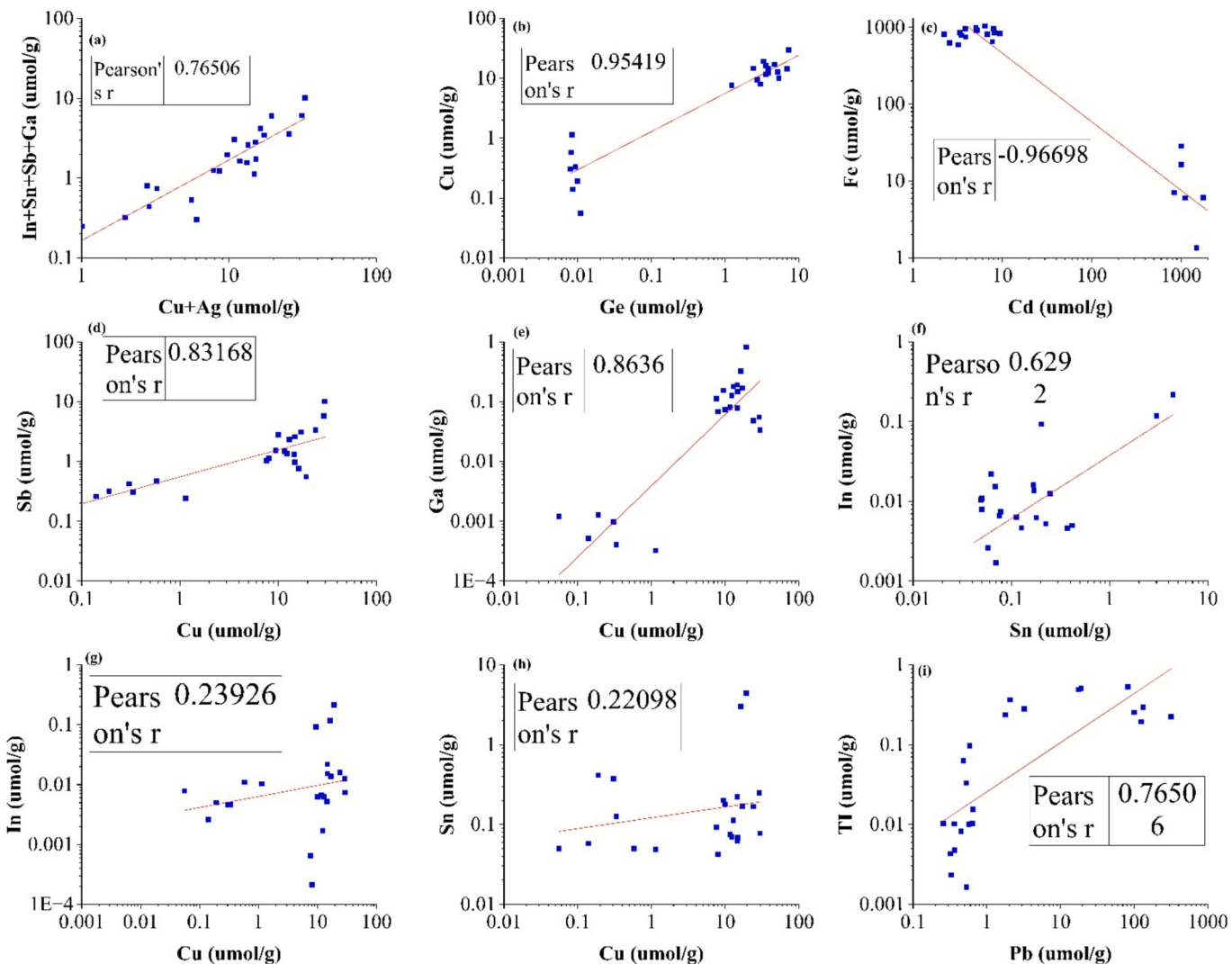


**Fig. 15.** Biplots of minor and trace elements in sphalerite-I from Gunga Pb-Zn deposit showing the correlation between different components and suggested substitution mechanisms.

the primary elements showed a negative correlation between the concentrations of Zn and Fe (Fig. 15), indicating that Fe directly replaced Zn ( $Zn^{2+} \leftrightarrow Fe^{2+}$ ). Despite the lack of a link between Cd, Zn, and Fe (Fig. 15) given their comparable geochemical properties, it was proposed that Cd directly replaced “Zn ( $Zn^{2+} \leftrightarrow Cd^{2+}$ )” during this sphalerite stage. Because the ionic radii of Mn, Co, and Hg are comparable to those of Zn, it has been proposed that these divalent elements typically substitute Zn directly in tetrahedral positions, even though there is no clear relationship between them (Cook et al., 2009; George et al., 2015; Zhang et al., 2022; Li et al., 2023a, 2023b).

Previous studies elucidate that Ge occurs in both forms, namely as a solid solution and as nanoscale inclusions in sphalerite, particularly in low-temperature deposits such as CD-type or MVT-type (Li et al., 2023; Fougerouse et al., 2023; Huston and Bastrakov, 2024). Given that Ge typically exists as  $Ge^{4+}$  in sphalerite, two substitution processes have been proposed for regulating Ge incorporation. Initially, a link between Cu and Ge was found, particularly in sphalerite patches that were rich in Ge and had Cu concentrations  $>10$  ppm. Therefore,  $3Zn^{2+} \leftrightarrow 2Cu^{+} + Ge^{4+}$  represents a promising alternative. This indicates that monovalent elements such as  $Cu^{+}$  and  $Ag^{+}$  are required for this situation (Belissont et al., 2016; Frenzel et al., 2016; Zhang et al., 2022; Li et al., 2023a). Second, in several deposits and samples, it appears that some Ge-rich spot analyses did not correspond to Cu. The major process of Ge

ingestion has been postulated to be  $2Zn^{2+} \rightarrow Ge^{4+} +$  (vacancies). According to our findings, Ge and Cu show a positive association, suggesting that  $3Zn^{2+} \leftrightarrow 2Cu^{+} + Ge^{4+}$  is a coupled substitution process.

The results of the LA-ICP-MS analysis of Cu, Sb, and Ga revealed slopes parallel to the corresponding molar ratios of “(Sb/Cu) and (Ga/Cu)”, suggesting a positive correlation between these elements (Fig. 15). The feasible substitution processes for these elements include the  $2Zn^{2+} \leftrightarrow Cu^{+} + Sb^{3+}$  and  $2Zn^{2+} \leftrightarrow Cu^{+} + Ga^{3+}$  reactions, as reported in previous studies (Cook et al., 2009; Zhang et al., 2022; Li et al., 2023a). Although the exact oxidation state of Sn remains a subject of debate, it is commonly found in sphalerite crystals, often in the form of  $Sn^{4+}$  (Belissont et al., 2016; Frenzel et al., 2016; Zhang et al., 2022; Li et al., 2023a). In addition, we found that the trace element compositions of Sn and In were positively correlated, as shown in Fig. 15. Additionally, we noted a minor correlation between copper and tin, as well as between copper and indium (Fig. 15). Based on these findings, it is proposed that Sn exists as a tetravalent ion that can be substituted by  $4Zn^{2+} \leftrightarrow Cu^{+} + In^{3+} + Sn^{4+} + \square$  (vacancy).

Belissont et al. (2016) provide more support for this claim.  $Cu^{+}$  and  $Ag^{+}$ , which are two monovalent cations, exhibit strong connections with trivalent or tetravalent cations, as shown in Fig. 15. This suggests that the incorporation of these trace elements may be caused by monovalent cations that balance the charge during this process. This theory is further

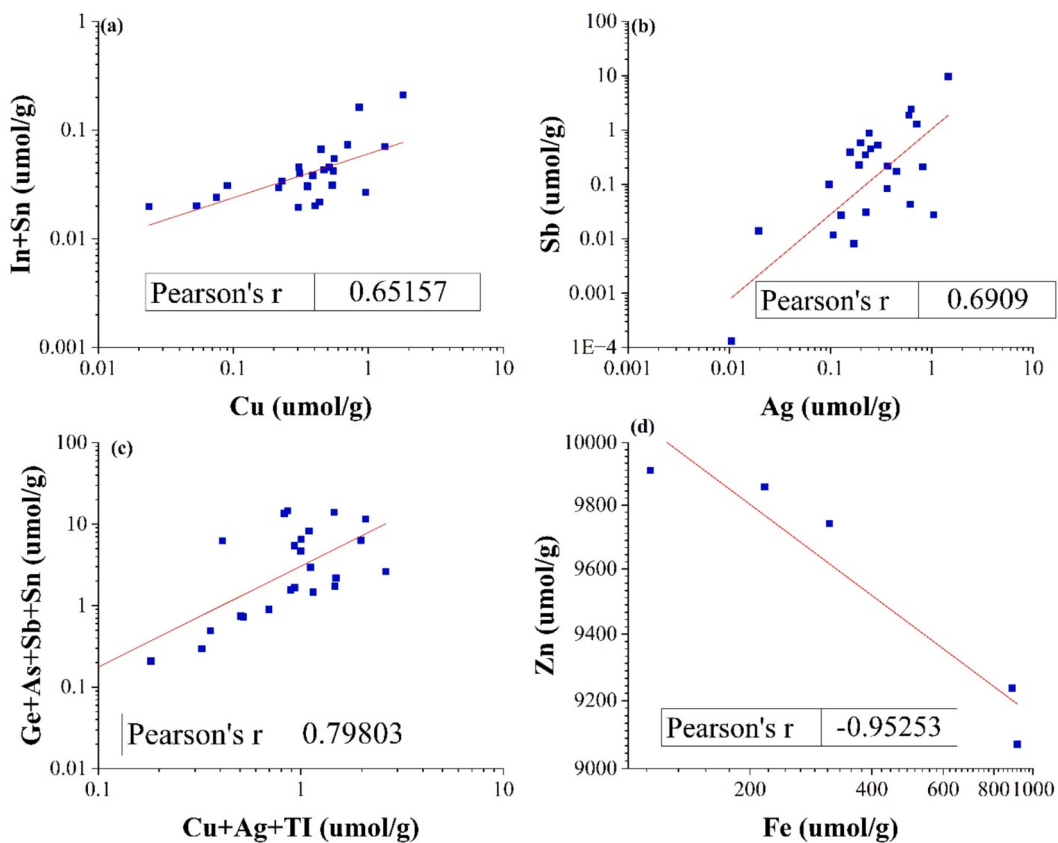


**Fig. 16.** Biplots of minor and trace elements in sphalerite-II from Gunga Pb-Zn deposit showing the correlation between different elements and suggested substitution mechanisms.

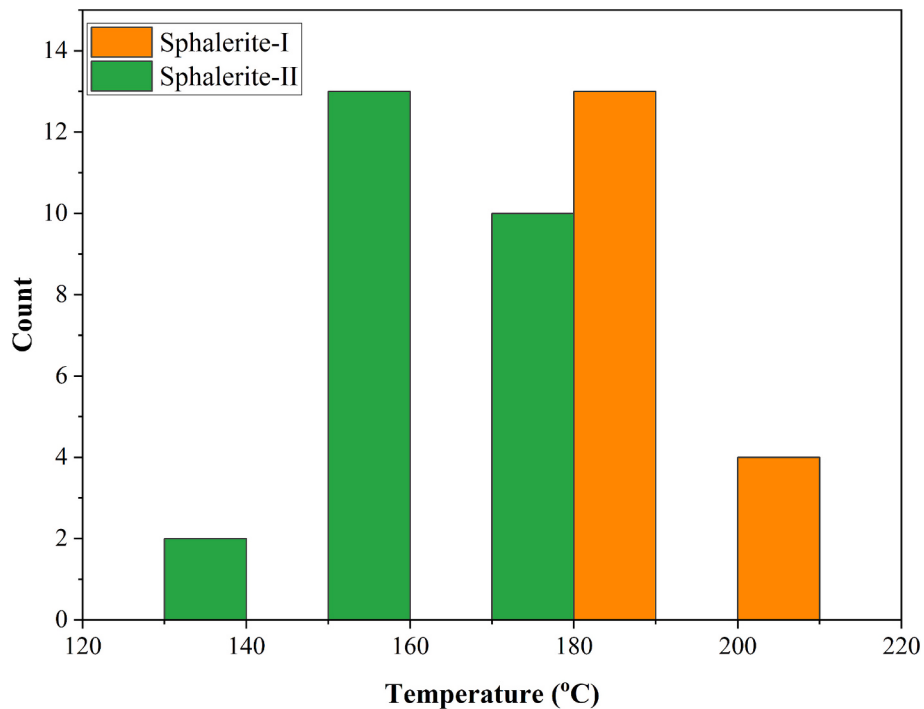


**Fig. 17.** Mineralization temperature calculated by geothermometer suggested by [Frenzel et al. \(2016\)](#) using trace elements concentration in sphalerite.

supported by the strong link between lead and thallium levels, as shown in prior research ([Fig. 15](#)).

#### 6.1.2. Sphalerite II (UMZ)

Our findings for the primary elements showed a negative correlation between the concentrations of Zn and Fe ([Fig. 16](#)), indicating that Fe

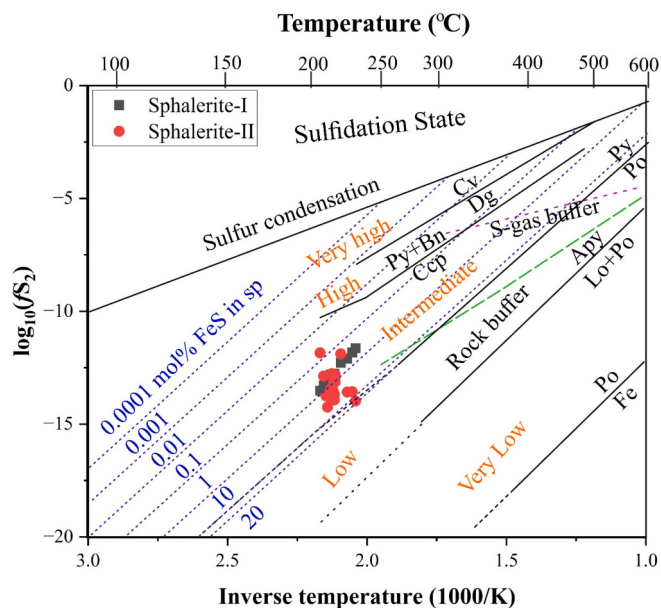


**Fig. 18.** Sulfur fugacity vs inverse temperature plot modified from Hedenquist (2003) and Frenzel et al. (2022) showing the position of sphalerite from Gunga deposit in relation to different mineral reactions (solid black lines), S-gas (purple dash lines), rock buffers (green dash lines) and Fe content in sphalerite (blue lines). Abbreviations: Bn: bornite, Cv: covellite, Dg: digenite, Fe: native iron, Lo: lollingite, Ccp: chalcopyrite, Apy: arsenopyrite, Po: pyrrhotite, Py: pyrite. (For interpretation of the references to color in this figure legend, the reader is referred to the web version of this article.)

directly replaced Zn ( $Zn^{2+} \leftrightarrow Fe^{2+}$ ). It has been proposed that Cd replaces Fe during this stage of sphalerite formation, despite the strong association between Cd and Fe. In addition to Zn, several other divalent elements such as Mn, Co, and Hg have been suggested to occupy tetrahedral positions as direct substitutes for Zn, given their comparable ionic radii (Cook et al., 2009; George et al., 2015; Zhang et al., 2022; Li et al., 2023a).

Two substitution processes have been proposed that likely govern the inclusion of Ge, because Ge typically exists in sphalerite as  $Ge^{4+}$ . First, there is a link between Cu and Ge, particularly in regions of sphalerite that are rich in Ge and contain Cu concentrations  $>10$  ppm. At this point, there was little association between Ge and Cu but there was a strong association with Ti. Our findings show a positive connection between Ge and Ti, suggesting that the linked substitution process is  $3Zn^{2+} \leftrightarrow 2Ti^{4+} + Ge^{4+}$  (Cook et al., 2009; George et al., 2015; Zhang et al., 2022; Li et al., 2023b). Sn is frequently observed in the sphalerite crystals, typically in the form of  $Sn^{4+}$ . However, the oxidation state of Sn remains an ongoing topic of research (Cook et al., 2009; George et al., 2015; Zhang et al., 2022; Li et al., 2023b). Researchers have noted positive trends in the trace element compositions of Sn + In and Cu, graphically represented in Fig. 16. These findings suggest that Sn may exist as a tetravalent ion that can substitute  $4Zn^{2+} \leftrightarrow Cu^{+} + In^{3+} + Sn^{4+} + \square$  (vacancy).

As shown in Fig. 16, our findings demonstrate a positive correlation between Ag and Sb, with their slopes nearly parallel to those of  $(Sb/Ag)_{\text{mol}} = 1$ . A possible coupled substitution mechanism is  $2Zn^{2+} \leftrightarrow Ag^{+} + Sb^{3+}$ . According to Cook et al. (2009), enrichment of trivalent and tetravalent cations (such as  $Ge^{4+}$ ,  $Sb^{3+}$ , As, and  $Sn^{4+}$ ), as well as monovalent cations (such as  $Cu^{+}$ ,  $Ag^{+}$ , and  $Ti^{4+}$ ), results from a generic linked substitution process. Fig. 16 shows the connection between trivalent/tetravalent and monovalent cations. This implies that the integration of these trace elements may have occurred since monovalent cations are the ones that keep the charge balance in this process.

## 6.2. Physicochemical conditions of Pb-Zn mineralization

### 6.2.1. Temperature of depositional environment

The relationship between the temperature of mineral formation and trace element content in sphalerite has been extensively studied and found to be closely linked. Consequently, the concentration of trace elements in sphalerite can serve as an indicator of ore-forming temperature (Frenzel et al., 2016; Li et al., 2023a, 2023b). Sphalerite, which is typically enriched in Fe, Mn, In, Sn, and Te, is believed to have formed under high-temperature conditions. In contrast, sphalerite formed at lower temperatures is enriched in Cd, Ga, and Ge, with a low In/Ge ratio.

Frenzel et al. (2016) developed a geothermometer based on trace elements in sphalerite that demonstrated a good correlation with fluid inclusion results. This geothermometer was applied to the Gunga deposit and the results are shown in Fig. 17. The geothermometer results for sphalerite-I and sphalerite-II range from 180 to 200 °C and from 130 to 180 °C, respectively, which is consistent with the temperature range of the non-magmatic sediment-hosted Pb-Zn deposits (100–250 °C). Analysis of sphalerite from the Gunga deposit revealed high concentrations of Cd and Ge, while In, Te, and Mn were low. This composition indicates a low-temperature formation environment, aligning with previous research findings (Jankovic, 1986). Based on these observations, we have concluded that the Gunga deposit likely formed under low-temperature conditions.

### 6.2.2. Sulfur fugacity

The influence of iron on the crystal structure of sphalerite is subject to changes in the temperature and oxygen conditions, as previously documented by Kelley and Jennings (2004) and Keith et al. (2014). Recently, Frenzel et al. (2022) developed a revised model for numerical modeling of fugacity ( $fS_2$ ) in sphalerite formed under low-temperature conditions. We applied this model to the sphalerite from the Gunga Deposit. The finding is that  $fS_2$  ranges between  $-11.63$  to  $-13.98$  and  $-11.9$  to  $-14.25$  in sphalerite-I and sphalerite-II, respectively (Fig. 18). Higher temperatures (180–200 °C), higher  $fS_2$ , and higher contents of Ge and Fe in sphalerite-I than in sphalerite-II suggest that either that the oxidation conditions became more oxidizing during the late stages of sulfide mineralization in the Gunga deposit, or the temperature decreased. Alternatively, both these factors may have played a role in this process.

### 6.2.3. Paleo-redox conditions

Under normal circumstances, redox conditions play a crucial role in determining the concentration of Mn in sphalerite. Sphalerite crystals with high Mn concentrations typically form in reduced environments (Kelley and Jennings, 2004; Li et al., 2023a). Sphalerite-I of the Gunga deposit displays a greater concentration of Mn in its sphalerite samples than that of sphalerite-II, which suggests that the initial stages of sulfide mineralization occurred in a relatively reduced environment.

## 6.3. Enrichment of Ge

Research has shown that the main factor influencing Ge enrichment is the Ge concentration in the ore-forming fluid, which directly impacts the amount of Ge incorporated into sphalerite during mineralization. Moreover, other factors, such as physicochemical conditions during mineralization, also play a crucial role in determining Ge enrichment. Through analysis of trace and minor element concentrations in sphalerite, we successfully determined the temperature and sulfur fugacity of the ore formation process (Niu et al., 2023; Miao et al., 2023; Meng et al., 2024).

Niu et al. (2023) suggested that sulfur fugacity, rather than temperature, is more critical in determining the Ge content in sphalerite. The main Ge compounds transported in aqueous hydrothermal fluids are hydroxides ( $Ge(OH)_4$ ) and chlorides ( $GeCl_4$ ) (Niu et al., 2023; Huston and Bastrakov, 2024). Due to TSR and BSR processes, the fluid's sulfate is

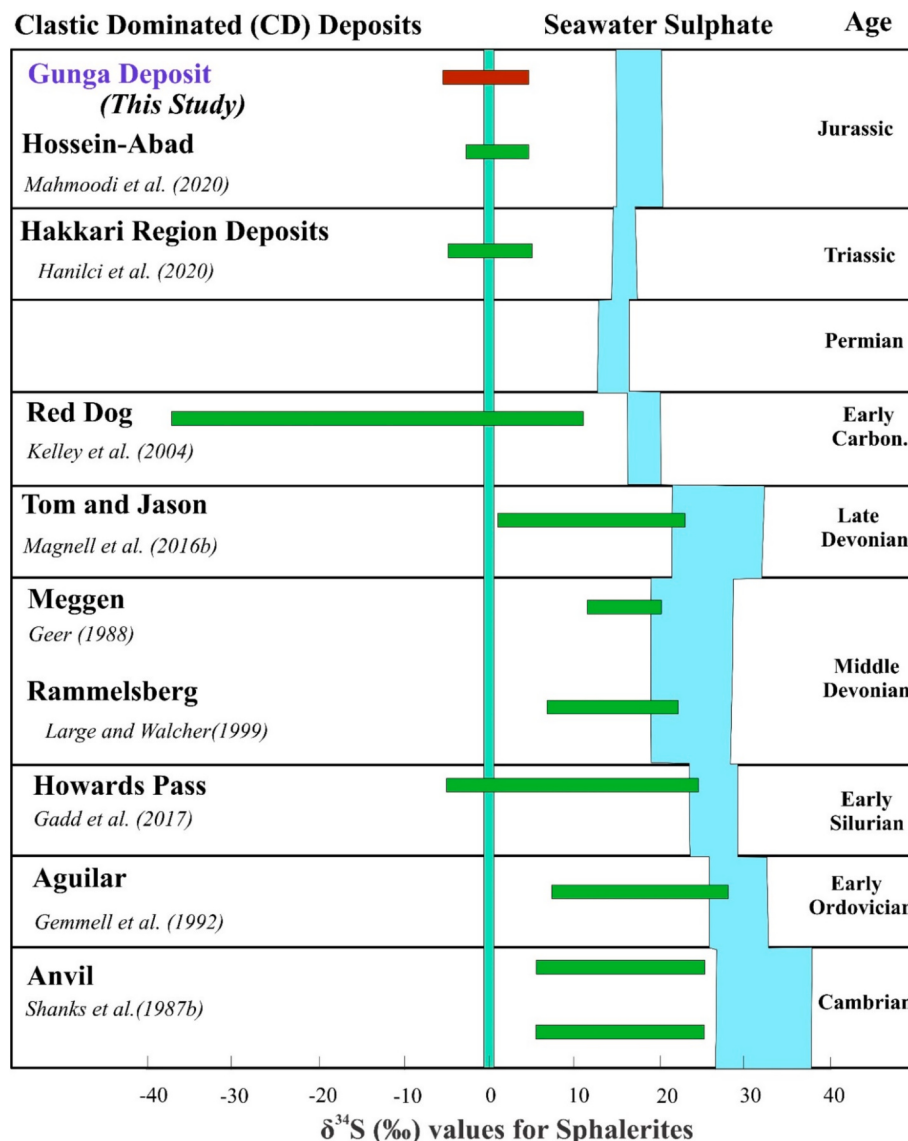


**Fig. 19.** S isotope compositions in Sphalerite from Gunga Deposit compared with different Phanerozoic SEDEX/CD Pb-Zn deposits of Central Tethyan Domain.

continuously transformed into reduced sulfur ( $\text{S}^{2-}$ ), indicating that higher sulfur fugacity results in increased reduced sulfur levels. As a result, elevated  $\text{S}^{2-}$  content binds  $\text{H}^+$  in the fluid, causing a rise in pH and enhanced  $\text{Ge(OH)}_4/\text{GeCl}_4$  concentrations in hydrothermal fluids, as described by the reactions  $\text{Ge}^{4+} + 4\text{OH} \leftrightarrow \text{Ge(OH)}_4$  and  $\text{Ge}^{4+} + 4\text{Cl}^- \leftrightarrow \text{GeCl}_4$  (Niu et al., 2023; Miao et al., 2023; Meng et al., 2024). The Gunga deposit displays varying sulfur fugacity and geochemical contents between sphalerite-I and sphalerite-II, with sphalerite-I exhibiting higher sulfur fugacity and Ge content, whereas sphalerite-II has a lower sulfur fugacity and Ge concentration. This pattern aligns with the previously discussed sulfur fugacity concept. Therefore, the higher Ge content in ore fluids, lower temperature, and higher sulfur fugacity are the main factors controlling the enrichment of Ge in the Gunga deposit.

#### 6.4. Sources of S

Details about the potential sources of sulfur and other metallogenic elements in deposits containing sulfide may be revealed by the isotopic composition ( $\delta^{34}\text{S}$  values) of minerals such as sulfide, sulfate, and/or ore-forming fluids ( $\delta^{34}\text{S}_{\text{SE}}$ ). Ohmoto (1972) explained the origin of minerals in ore deposits using sulfur isotopes. Variables that affect the isotopic composition of hydrothermal minerals include the temperature,

$f_{\text{O}_2}$ , pH, and isotopic composition of the ore-forming fluids. While the first two concern the conditions surrounding the deposition, the latter identifies the source of sulfur (Ohmoto, 1972; Mahmoodi et al., 2021).

Analyzing mineral deposits using isotope analysis can yield important information about the geochemical processes that generate these deposits. Globally, the range of  $\delta^{34}\text{S}$  values for sulfide minerals in CD deposits is -5 to 25 ‰ (Leach et al., 2005). The isotope compositions of sulfides from the Phanerozoic CD deposits are shown in Fig. 17. As Fig. 17 illustrates, the  $\delta^{34}\text{S}$  values of ore sulfides in the Gunga Pb-Zn deposit (-10 to +5) are within the global range of values seen in CD deposits, which range from -30 to +25 ‰.

In most diagenetic environments, the chemical reaction between dissolved sulfate and hydrocarbons is thermodynamically unstable. This instability results in redox reactions where hydrocarbons act as reducing agents for sulfate. This can occur through BSR or TSR, both of which produce geologically and economically important byproducts.

The BSR is effective within a temperature range of 0 to approximately 60–80 °C. Above this threshold, most sulfate-reducing bacteria become inactive. Although some hyperthermophilic microbes are capable of generating  $\text{H}_2\text{S}$  at higher temperatures, they are rare and typically not found in geological settings conducive to BSR. On the other hand, TSR commonly occurs between 100 and 140 °C, although some

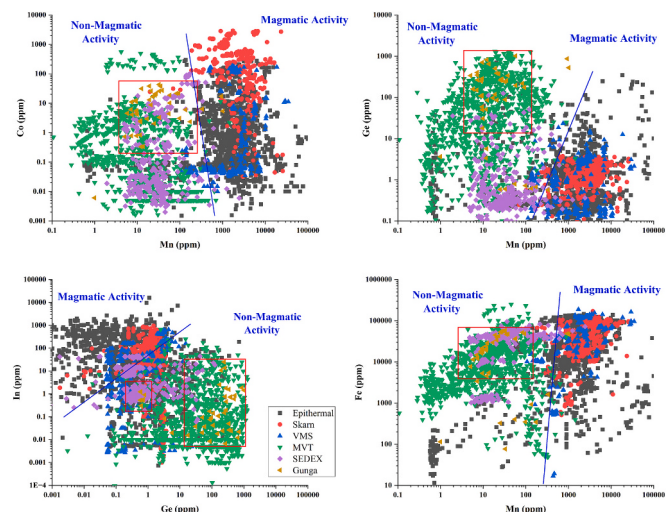


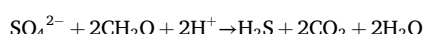
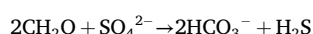
**Fig. 20.** Biplots of minor and trace elements from different Pb-Zn deposits for Metallogenetic discrimination. Magmatic origin deposits like Epithermal, Skarn and VMS are clearly separated from non-magmatic deposits like MVT and SEDEX. Gunga deposit lies in non-magmatic region with SEDEX and MVT.

environments may require temperatures between 160 and 180 °C. Various factors affect the initiation and progression of TSR, including the nature of organic reactants, the presence of substances that inhibit or accelerate kinetics, the speed at which anhydrite dissolves, surface wettability characteristics, and the rates at which major reactants move and spread.

The reaction kinetics of BSR and TSR also differed significantly. BSR proceeds rapidly in most geological environments, making it geologically instantaneous. In contrast, TSR occurs at a slower pace, but it is still geologically significant. Over periods ranging from tens of thousands to several million years, this process has the potential to create sour gas reservoirs and MVT deposits within a temperature range of 100–140 °C.

For BSR, the main organic substrates are organic acids and other products resulting from aerobic or fermentative degradation processes. In the case of TSR, the principal reactants consist of branched and linear alkanes, followed by cyclic and monoaromatic compounds within the gasoline range. The primary source of sulfate is the dissolution of gypsum and/or anhydrite, which can be found as either primary or secondary deposits in proximity to the redox reaction locations.

Although BSR and TSR yield similar byproducts, their proportions can vary significantly depending on local conditions, such as the availability of reactants, the chemistry of the formation water, and wettability (Machel, 2001). According to Machel et al. (1995), the two usual responses for TSR and BSR are as follows:



Studies conducted by Claypool et al. (1980) and Kampschulte and Strauss (2004) revealed long-term variations in seawater sulfate  $\delta^{34}\text{S}$  values by examining the composition of sulfate minerals in marine evaporites. The sulfate values for Jurassic seawater ranged between  $\delta^{34}\text{S}$  14 to 22 ‰, as reported by Claypool et al. (1980) and Kampschulte and Strauss (2004), with a narrower range of 15 to 17 ‰, as stated by Bottrell and Newton (2006). Assuming the source of sulfur to be Jurassic seawater (14 to 22 ‰) and considering the minimum isotopic fractionation for BSR (which varies between 20 and 70 ‰ with an average of 50 ‰) and TSR (which varies between 10 and 20 ‰ with an average of 15 ‰), the minimum seawater sulfate  $\delta^{34}\text{S}$  value would have been approximately -3 ‰ and +2, respectively. The sphalerite samples from the Gunga Zn-Pb deposit in sphalerite-I had negative  $\delta^{34}\text{S}$  values (-10 to -1.0 ‰: avg. -3.89 ‰), whereas samples from sphalerite-II exhibited a

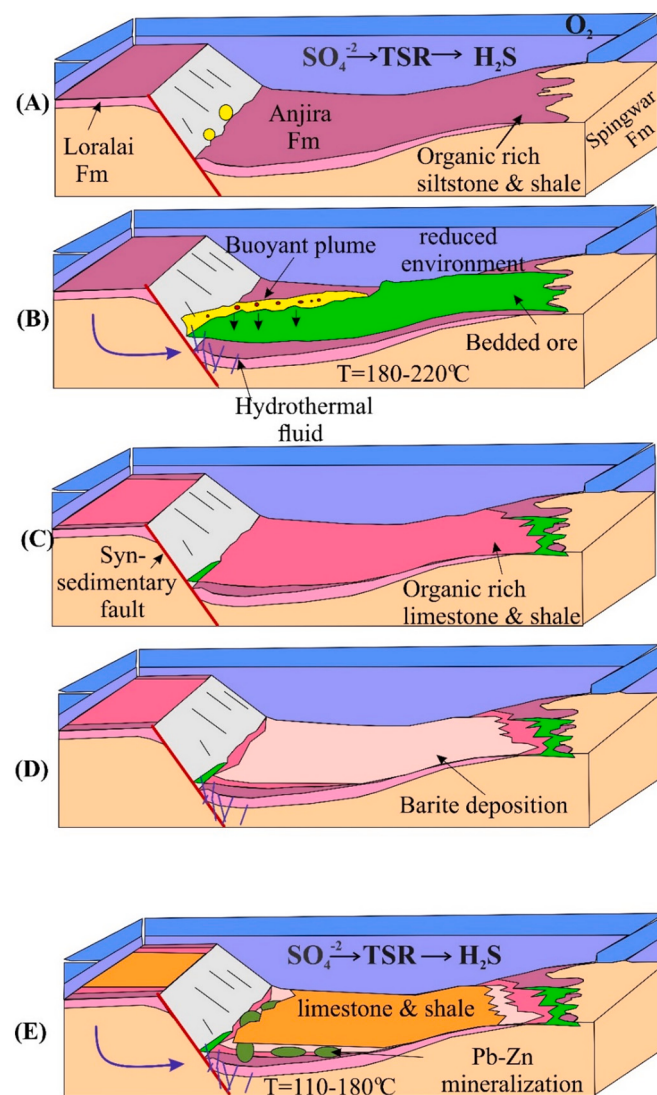


**Fig. 21.** Depositional environment for Gunga Pb-Zn deposit in Rift segment of extensional tectonic settings: (A–C) Exhalation of metal bearing hydrothermal fluid on the seafloor and precipitation of ore metals before diagenesis during Jurassic Period (D–E) Further upward flow of hydrothermal fluid and deposition of Barite and massive sulfide ore minerals during diagenesis.

range of positive values (3.1 to 5.6 ‰: avg. +3.94). The Gunga Zn-Pb data suggest that the BSR was the main source of sulfur of sphalerite-I, and the TSR sources were responsible for the sphalerite-II formation. For sphalerite-I, when combined with low formation temperatures, this suggests that bacterial sulfate reduction (BSR) is the main sulfate reduction mechanism. Furthermore, the presence of frambooidal pyrite, high TOC values, and low-temperature elements in the sphalerite supports this conclusion.

Moreover, the thermal breakdown of pyrite in shale (e.g., Jurassic shales) may have produced light isotopes. One important source of reduction is pyrite leaching in faulted shale-limestone contacts close to the mineralization location. The mineralization temperature results for sphalerite-I and sphalerite-II range from 180 °C to 210 °C and 130–180 °C respectively, which is inconsistent with the temperature range of the BSR (max. 110 °C). However, the BSR process may occur at different locations or times (Cooke et al., 2000; Leach et al., 2005; Jazi et al., 2017).

The discovery of a large, strata-bound barite mineral in the upper horizon with  $\delta^{34}\text{S}$  values ranging from 20 to 43 ‰, with an average of 34 ‰, is inconsistent with the Jurassic sulfate values (14–22 ‰) (Claypool

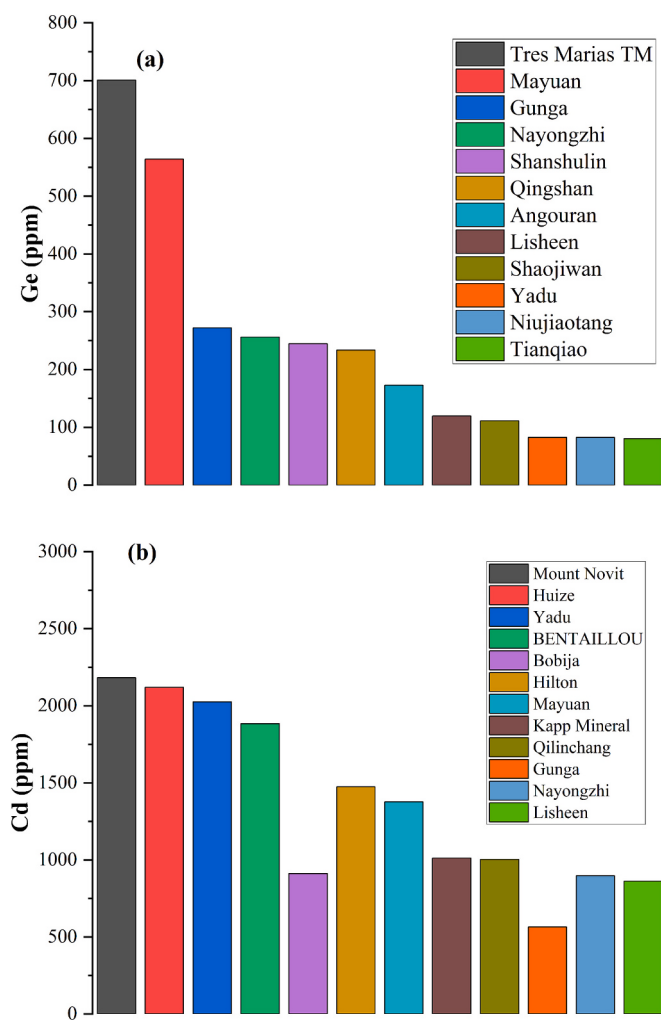


**Fig. 22.** Comparison of average concentrations of Ge and Cd of Gunga Deposit with sediment-hosted deposits.

et al., 1980)). It is proposed that the barite originated from the underlying Cambrian or Precambrian evaporites, which were thought to be present in the basement rocks of the Indian Plate. These evaporites were subjected to extraction by basinal brines that circulated through the rocks due to tectonic activity. Husain et al. (2002) also suggested that Barite from Gunga deposit is epigenetic in origin and is a strata-bound hydrothermal deposit (Fig. 19).

### 6.5. Sources of Pb

One useful geochemical marker for identifying the source of metals in ore deposits is the analysis of Pb isotopes in sulfides. Table 3 shows that the Pb isotopes in the sulfide minerals from the studied region had a constant chemical composition. The maximum analyzed samples were tightly clustered above the typical upper crustal Pb evolution line in the Pb isotope evolution diagram created by Zartman and Doe (1981) (Fig. 12a). In contrast, in Fig. 12b, the maximum analyzed samples were clustered near the orogen curve. These results indicate diverse sources of Pb. These differences could be the result of several crustal sources that led to ore mineralization. Nonetheless, the ultimate source of Pb was crustal, similar to other Pb-Zn deposits in the Central Tethyan region. The high  $^{206}\text{Pb}/^{204}\text{Pb}$  ratios during mineralization, as inferred from the computed  $\mu$  values, also indicate the presence of crustal Pb sources (Zartman and Doe, 1981). The surrounding or underlying lithology of the deposits may be reflected in Pb isotope measurements. These findings suggest that the Zn mineralization in the Gunga deposit originated from crustal materials. The Pb isotope values of the Gunga deposit follow the same trend as those of SEDEX deposits worldwide (Leach et al., 2005; Hoggard et al., 2020).

### 6.6. Ore genesis

Recent studies have shown that deposits of Ge and Cd are more commonly found in association with low-temperature hydrothermal fluids that lack a clear connection to magmatic-hydrothermal activity, whereas In is more commonly found in deposits with a magmatic connection (Cook et al., 2009; George et al., 2015; Zhang et al., 2022; Li et al., 2023b). In addition, various deposit types exhibit distinct Zn/Cd ratios (Wen et al., 2016; Spry et al., 2022). The Ga levels in the sphalerite within the different deposit types did not vary significantly, except for depletion in the SEDEX and skarn deposits. Ga is often found in sphalerite within Pb-Zn deposits in natural environments; however, the mechanism by which it is incorporated into sphalerite remains a topic of debate among researchers. According to some studies, sphalerite generated from low-temperature, non-magmatic hydrothermal deposits tends to have a higher Ga concentration. The initial elemental concentrations of the ore-forming fluid and the internal geochemical behavior of Cd, Ga, Ge, and In affect the fluctuations in the sphalerite content (Cook et al., 2009; George et al., 2015; Zhang et al., 2022; Li et al., 2023b).

To gain a deeper understanding of the geochemical behavior of elements in the Gunga deposit, we created binary plots based on information from prior studies. According to these studies, sphalerite, which is commonly found in magmatism-related deposits such as epithermal, skarn, CRD, and VMS deposits, often exhibits high levels of In, Mn, and Co, as well as low levels of Ge and Cd. In contrast, sphalerite found in CD deposits tends to have low levels of Mn, In, Co, and Ga, and high levels of

**Table 1**  
Major elements concentration (wt%) in sphalerite from Gunga Deposit.

S no.	Zn	Fe	Pb	S	Cd	Mo	Ga	Cu	Total
1	64.29	1.79	bdl	32.17	0.12	0.53	0.10	bdl	99.00
2	60.96	5.06	bdl	32.81	0.10	0.50	0.08	0.01	99.53
3	65.41	0.65	0.01	32.53	0.05	0.53	0.03	bdl	99.20
4	59.87	5.21	bdl	32.72	0.14	0.54	0.13	bdl	98.61
5	65.06	1.24	bdl	32.07	0.04	0.56	0.12	bdl	99.09
6	60.96	5.06	bdl	32.81	0.10	0.50	0.08	0.01	99.53
7	65.41	0.65	0.01	32.53	0.05	0.53	0.03	bdl	99.20
8	64.29	1.79	bdl	32.17	0.12	0.53	0.10	bdl	99.00
9	59.87	5.21	bdl	32.72	0.14	0.54	0.13	bdl	98.61
10	60.96	5.06	bdl	32.81	0.10	0.50	0.08	0.01	99.53
11	60.96	6.00	bdl	32.12	0.14	0.07	bdl	bdl	99.83
12	60.04	5.67	bdl	32.01	0.04	0.05	bdl	bdl	98.20
13	60.05	5.50	bdl	32.72	0.10	0.10	bdl	bdl	98.65
14	60.07	5.05	bdl	32.72	0.10	0.07	bdl	bdl	98.70

**Table 2**

Minor and trace elements concentration (ppm) for Lower and Upper Mineralized zones of Gunga Deposit.

S.no	Mineral	V	Cr	Mn	Fe	Co	Ni	Cu	Ge	As	Se	Mo	As	Pd	Cr	Sn	Sp	Tl	Ba	Hg	Li	qd			
21	Sphalerite-I	0.55	297.04	55.32	403.20	4.42	1.86	3.62	0.09	0.79	14.59	15.65	0.00	102.21	92,896.30	0.91	5.91	22.85	0.27	0.10	61.40	103.79	3978.03		
		0.80	7.22	33.14	76.60	3.29	1.35	74.37	0.02	0.60	10.00	0.53	0.26	520.93	166,342.30	1.19	5.77	29.49	0.07	0.00	50.95	100.48	3672.21		
		0.72	607.99	25.20	326.15	2.05	1.76	37.65	0.00	0.58	10.33	2.01	0.93	533.61	257,857.10	1.26	5.93	57.01	0.23	0.03	30.56	108.99	17,203.28		
		0.92	42.18	174.23	344.19	2.35	1.18	21.68	0.03	0.67	11.70	2.57	bdl	271.16	124,337.77	0.53	14.94	37.04	0.04	0.54	28.63	39.75	25,785.11		
		1.15	17.57	332.49	1614.96	6.37	4.68	19.84	0.07	0.57	14.91	2.88	bdl	264.63	111,438.65	0.53	44.07	51.04	bdl	177.38	31.95	45.82	66,258.50		
		0.72	105.38	97.99	349.01	3.07	1.25	12.37	0.09	0.72	10.49	1.96	bdl	326.97	196,806.94	0.57	48.96	38.31	bdl	2.03	21.36	52.26	20,871.50		
		1.16	675.10	135.84	927.12	6.01	2.61	9.09	0.04	0.62	12.56	5.05	bdl	195.92	111,036.57	0.30	6.80	31.52	bdl	7.73	19.72	60.50	27,467.33		
		bdl	3.35	25.99	52,304.81	18.90	bdl	758.35	5.74	258.02	9.08	1.87	bdl	23.10	581.08	0.76	8.90	177.96	bdl	bdl	69.12	2.13	53.19		
		bdl	4.22	27.88	55,446.20	21.32	bdl	957.00	10.53	275.68	23.43	3.11	0.16	44.77	560.34	1.76	8.12	313.22	bdl	0.07	69.41	3.16	134.63		
		bdl	1.98	19.32	44,632.93	13.02	bdl	947.64	13.57	500.57	12.24	bdl	0.07	65.85	386.90	0.60	26.41	159.25	bdl	bdl	61.94	12.91	100.18		
		3.61	590.26	1018.99	46,603.45	5.40	bdl	1927.32	2.40	523.76	157.22	bdl	0.34	324.40	246.03	0.85	9.13	1216.86	bdl	1.25	103.64	58.09	669.83		
		0.07	5.73	57.73	35,595.42	10.22	bdl	1889.07	3.90	1014.89	89.14	bdl	0.25	222.33	284.43	1.43	29.28	696.76	0.30	0.63	60.39	74.70	430.23		
		3.92	105.74	937.88	48,339.29	17.18	bdl	1561.75	3.40	864.77	52.26	bdl	0.04	161.81	371.97	1.85	19.75	403.38	bdl	2.68	87.36	48.64	371.65		
		0.02	1.89	23.16	42,554.44	16.67	bdl	840.55	12.66	373.67	17.16	1.19	bdl	55.76	431.75	0.72	13.27	279.95	bdl	bdl	54.41	6.79	109.74		
		0.13	4.01	93.37	48,406.08	21.65	bdl	954.91	5.53	174.37	7.54	1.68	bdl	18.28	901.19	2.53	7.32	117.12	bdl	bdl	78.47	2.06	119.18		
		4.55	32.38	54,248.60	43.38	bdl	1251.65	57.95	239.03	1.37	0.49	bdl	25.84	881.48	24.87	522.46	67.00	bdl	bdl	52.65	0.88	66.26			
		0.11	17.50	83.37	51,747.45	21.59	bdl	522.68	4.81	217.67	7.82	2.13	bdl	57.87	566.52	0.02	4.99	136.63	bdl	bdl	56.79	2.08	75.18		
		0.01	6.68	26.66	54,709.72	21.02	0.24	799.98	9.04	275.93	10.80	2.63	bdl	99.91	427.12	0.19	8.25	164.97	bdl	bdl	67.38	2.13	132.11		
		bdl	11.60	32.84	59,203.25	25.78	0.04	496.50	7.92	88.23	8.32	2.10	bdl	21.53	710.25	0.07	10.94	126.00	bdl	0.17	53.16	0.48	68.19		
		0.01	18.46	38.33	47,621.25	27.27	0.04	1109.09	11.93	338.47	26.36	2.20	bdl	30.94	1036.08	1.57	20.06	374.73	bdl	1.43	58.40	0.97	76.11		
		0.61	3.67	57.99	36,954.15	18.78	0.52	613.18	10.91	195.60	11.65	2.33	bdl	30.83	858.13	10.69	23.78	183.68	bdl	bdl	55.67	1.68	93.03		
		0.12	5.97	35.39	46,194.22	37.81	bdl	1055.85	23.09	256.71	7.79	0.88	bdl	12.17	748.21	13.63	354.14	92.02	bdl	bdl	53.89	0.34	110.52		
		0.00	3.48	20.90	33,633.43	8.78	bdl	652.00	5.21	386.75	19.39	3.26	bdl	86.02	356.24	0.72	21.22	339.69	bdl	0.55	45.90	19.80	121.84		
		Median	0.58	7.22	38.33	44,632.93	16.67	1.25	758.35	5.21	239.03	11.70	2.13	0.21	86.02	748.21	0.85	13.27	136.63	0.23	0.59	55.67	12.91	132.11	
		1	Sphalerite-II	-0.11	27.22	0.99	114.62	0.01	2.77	1.54	40.80	3.63	0.35	bdl	bdl	2.08	854.72	bdl	2.34	1.69	0.41	272.40	61.30	0.21	3.20
		2		0.58	32.53	12.25	4573.06	0.33	1.59	19.69	0.51	821.07	210.05	0.14	bdl	16.68	272.32	bdl	2.30	47.58	bdl	112.64	119.37	82.69	497.90
		3		0.61	51.06	12.09	20,859.28	2.56	1.73	4.88	3.43	5.65	0.42	2.91	bdl	10.31	506.38	0.02	2.82	12.11	bdl	46.09	82.76	2.10	24.72
		4		0.50	38.03	7.28	3371.77	0.78	0.82	35.79	5.02	402.18	163.19	0.17	0.33	26.64	371.81	0.02	4.92	54.99	bdl	600,630.19	89.82	61.14	21,163.28
		5		0.47	32.26	9.62	5277.96	0.78	0.67	22.99	1.08	705.53	273.10	bdl	0.06	31.24	298.95	0.02	3.55	63.85	bdl	10,357.34	97.36	167.35	472.93
		6		0.30	34.98	5.08	7676.56	0.73	0.82	19.94	2.42	338.12	39.90	bdl	0.01	48.17	365.07	0.05	5.33	20.96	bdl	3758.36	104.00	35.31	138.09
		7		0.11	168.32	16.91	29,452.08	2.96	1.36	33.40	7.01	96.62	6.46	bdl	0.79	38.68	563.02	0.09	5.27	10.11	bdl	bdl	126.72	3.02	1656.45
		8		0.88	30.87	13.67	5440.56	0.34	0.58	28.31	1.61	648.58	292.55	bdl	0.03	21.23	248.96	0.01	2.56	70.76	bdl	1212.80	114.98	40.06	640.26
		9		0.31	18.41	9.70	18,272.28	5.61	0.33	14.10	7.88	17.87	0.65	bdl	0.04	11.33	506.73	0.02	3.46	1.43	bdl	bdl	90.74	0.24	138.97
		10		0.44	36.10	9.61	20,596.18	4.42	0.21	22.81	19.83	49.58	0.05	bdl	18.11	521.41	0.02	3.60	0.99	bdl	bdl	125.36	0.24	31.91	
		11		0.33	16.98	7.51	12,023.51	4.08	0.45	35.18	9.12	263.36	57.75	0.64	bdl	39.05	420.55	0.01	3.67	26.40	bdl	bdl	137.33	18.63	124.09
		12		0.26	15.69	9.95	17,628.50	4.16	0.14	14.87	7.84	30.59	0.49	1.08	bdl	13.61	411.12	0.04	3.98	3.30	bdl	bdl	92.83	0.48	835.33
		13		0.28	15.20	7.10	14,655.00	6.10	-0.10	29.00	11.65	149.70	0.49	bdl	bdl	111.81	380.24	0.02	7.85	3.34	bdl	bdl	92.30	0.09	5.64
		14		0.32	12.45	11.77	19,182.39	0.83	0.39	3.48	12.42	3.34	0.36	bdl	bdl	1.12	409.41	0.08	2.29	0.02	bdl	bdl	63.05	0.01	1.92
		15		0.33	22.47	5.81	11,401.27	4.55	0.21	117.82	11.56	158.05	1.04	bdl	bdsl	86.86	379.55	0.11	24.70	25.36	bdl	bdl	95.19	0.56	50.65
		16		0.28	19.45	9.45	21,342.42	5.32	0.32	30.49	33.63	58.87	0.46	bdl	bdl	23.94	446.35	0.04	5.03	3.75	bdl	9.37	67.61	0.77	336.40
		17		0.44	12.65	11.84	24,263.63	2.33	0.09	25.13	18.13	50.90	bdl	bdl	12.68	423.72	0.09	4.42	0.06	bdl	4.83	59.00	0.02	17.74	
		18		0.12	23.87	9.41	18,896.01	5.57	-0.04	55.63	18.33	110.14	0.68	bdl	bdsl	65.45	406.24	0.14	19.00	5.18	bdl	5.63	37.83	0.55	215.45
		19		0.37	46.40	9.19	16,238.74	12.04	0.48	20.15	3.91	245.71	48.54	bdl	bdsl	66.96	640.58	0.15	4.58	296.58	bdl	13.89	118.26	13.93	310.43
		20		1.08	128.76	9.45	18,311.44	11.38	0.61	86.15	7.26	283.47	34.04	bdl	0.78	63.43	599.13	0.46	7.84	229.13	bdl	16.60	146.10	12.73	219.45
		21		2.14	23.05	7.32	12,551.16	11.02	0.28	5.86	0.72	347.34	40.09	0.09	0.88	25.79	448.20	0.03	3.62	106.60	bdl	3.90	67.66	16.14	337.50
		22		0.65																					

**Table 3**

Sulfur isotope compositions of Sphalerite and Barite from Gunga deposit.

S. no.	Mineral	$\delta^{34}\text{S}_{\text{v}}.$ CDT	Mineral	$\delta^{34}\text{S}_{\text{v}}.$ CDT	Mineral	$\delta^{34}\text{S}_{\text{v}}.$ CDT
1	Sphalerite-I	-1.62	Sphalerite-II	3.89	Barite	34.71
2		-2.02		5.15		39.66
3		-0.74		4.97		24.72
4		-4.14		3.74		18.77
5		-2.41		5.64		41.58
6		-6.59		3.04		28.97
7		-0.90		3.88		23.40
8		-4.34		3.75		34.47
9		-5.63		3.21		30.16
10		-10.49		3.15		33.30
11				3.29		47.82
12				3.53		29.53
13						38.46
14						37.25
15						40.47
16						43.03
Average		-3.89			3.94	34.14

**Table 4**

Pb Isotope compositions of Sphalerite from Gunga deposit.

S. no.	Mineral	$^{208}\text{Pb}/^{204}\text{Pb}$	$^{207}\text{Pb}/^{204}\text{Pb}$	$^{206}\text{Pb}/^{204}\text{Pb}$
1	Sphalerite	38.71	15.68	18.54
2		38.71	15.68	18.54
3		38.74	15.71	18.56
4		38.70	15.68	18.54
5		38.73	15.70	18.56
6		38.74	15.71	18.57
7		38.71	15.68	18.54
8		38.71	15.68	18.54
9		38.53	15.61	18.46
10		38.74	15.68	18.54

**Table 5**

Results of Neural Network Model.

Accuracy FCNN (Scaled) = 94.72990777338603

## Classification report

	Precision	Recall	f1-Score	Support
0	0.96	0.92	0.94	277
1	0.98	0.97	0.97	251
2	0.91	0.98	0.94	60
3	0.85	0.96	0.9	78
4	0.98	0.92	0.95	93
Micro avg	0.95	0.95	0.95	759
Macro avg	0.93	0.95	0.94	759
Weighted avg	0.95	0.95	0.95	759
Samples avg	0.95	0.95	0.95	759

Ge and Cd (Cook et al., 2009; George et al., 2015; Zhang et al., 2022; Li et al., 2023b). The sphalerite found in the Gunga deposit displayed low levels of Mn, In, and Ga, consistent with the characteristics of sphalerite found in the CD deposits (Fig. 20), which is consistent with the results of the deep learning model.

Our research has revealed the primary characteristics of the Guna Pb-Zn deposit to be: i) The mineralization occurs within a Jurassic shelf margin sedimentary sequence, ii) The  $\delta^{34}\text{S}$  isotope compositions are typical of non-magmatic sources, ranging from -10 to +5 ‰, iii) The Pb content originates from upper continental crust and/or orogenic sources, iv) The mineralization occurred at a low temperature (<200 °C), v) There is no correlation with coeval igneous activity, as indicated by low levels of In, Mn, Ga, and high levels of Ge and Cd, and vi) The deposit is characterized by higher sulfur fugacity. These features align with the characteristics of CD-type mineralization (Fig. 21), as described by Leach et al. (2005).

**6.7. Implications for mineral exploration**

The geochemistry of various ore minerals, including scheelite, magnetite, pyrite, apatite, and chlorite, has been utilized in mineral exploration efforts. Geochemical vectors for exploration are provided by changes in trace element concentrations with depth or separation from the mineralization core. The application of sphalerite chemistry in mineral exploration is seldom reported, primarily due to insufficient data and a lack of distinguishing criteria. Determining the type of mineral deposit is the first stage of the indicator mineral approach. The capacity of deep learning algorithms to discriminate is tested using sphalerite, which has an unclear provenance.

The findings of applying the suggested models to differentiate between sphalerites with an unclear origin show that sphalerite chemistry may be utilized to identify a wide range of deposit types. Sphalerite discrimination may be helpful for the first screening during the course of mineral discovery. In the case of sphalerite, with an unknown source, we can rapidly determine the potential deposit types by analyzing the trace element composition of the sphalerite and incorporating it into machine learning models such as neural networks. The potential of Pb-Zn deposits for mineralization can be assessed using these findings. Additionally, some types of Pb-Zn deposits frequently contain essential metals, such as In, Ga, Ge, and Co. Thus, identifying deposit types that include sphalerite is important for assessing the resource potential of key metals.

**6.7.1. Ge**

The average concentration of germanium in the Earth's crust is 1.5 ppm, making it an essential semiconductor material with extensive applications in various fields, particularly in infrared photosensitivity. Ge is present in over 20 independent minerals, including argyrodite ( $\text{Ag}_8\text{Ge}_6$ ), renierite ( $(\text{Cu}, \text{Zn})_{11}(\text{Ge}, \text{As})_2\text{Fe}_4\text{S}_{16}$ ), briartite ( $\text{Cu}_2(\text{Zn}, \text{Fe})\text{GeS}_4$ ), and germania ( $\text{GeO}_2$ ), although it is generally dispersed in minerals composed of other elements. The main sources of Ge worldwide are sedimentary-hosted lead-zinc deposits, coal-lignite deposits, and carbonate metasomatic lead-zinc-copper deposits. In Pb-Zn deposits, Ge exists as an isomorphous solid solution as well as micro-or nanoscale inclusions in the sphalerite (Höll et al., 2007; Wen et al., 2020; Liu et al., 2023; Fougerouse et al., 2023; Wu et al., 2023; Huston and Bastrakov, 2024).

The concentration of germanium (Ge) in the sediment-hosted deposits varied from 20 to 500 ppm, with an average of 140 ppm in sediment-hosted deposits, as shown in Fig. 22. Specifically, the Tres Marias deposit had the highest Ge content, averaging 700 ppm, whereas the Sinkholmen deposit had the lowest Ge content, averaging 5 ppm. The Gunga deposit exhibits significant variation in Ge content, ranging from 50 to 1018 ppm in the lower mineralized zone, with an average of 374 ppm, and from 20 to 821 ppm in the upper mineralized zone, with an average of 207 ppm. This is notably higher than the average Ge content of other Ge-hosted SEDEX/MVT deposits. The Gunga deposit contains 2.1 % lead and 11.4 % zinc, indicating a significant potential for Ge metal production. Further research is required for its commercial production (Wen et al., 2020; Zhang et al., 2022; Li et al., 2023a, 2023b).

**6.7.2. Cd**

Cadmium (Cd) is an element commonly found in the Earth's crust, with an average abundance of 0.15 ppm, or 1 microgram per gram of rock. Lead-zinc deposits are the primary source of Cd resources on Earth, but the concentration of Cd varies significantly between different types of deposits. Sphalerite, a mineral found in MVT deposits, has the highest average Cd content (>4850 ppm), while CD deposits have a lower average content (2560 ppm), and other types of lead-zinc deposits, such as skarn deposits, have a moderate average content (<4100 ppm). In these lead-zinc deposits, Cd is mainly found as an associated metal in sphalerite and, in some cases, as inclusions in secondary zinc minerals,

such as hydrozincite, smithsonite, and lepidocrocite (CsS) (Wen et al., 2020; Li et al., 2023a). In the Gunga deposit, the Cd concentration ranges from 246 to 1036 ppm in the lower mineralized zone, with an average value of 584 ppm. The Cd content in other sediment-hosted deposits that host Cd typically ranges from 248 ppm to 1446 ppm, with an average value of 550 ppm (Fig. 22). The Gunga deposit (6.86mt) has a significant potential for Cd production and warrants further exploration for commercial production.

## 7. Conclusions

Sphalerite's high-dimensional trace element data can efficiently identify deposit type, but traditional two-dimensional plots complicate interpretation. Learning from sphalerite compositions via supervised machine learning effectively interprets these data and differentiates ore origins. The Gunga Pb-Zn deposit features two distinct mineralized zones: the Lower Mineralized Zone (sphalerite-I) with vein-style sphalerite, and the Upper Mineralized Zone (sphalerite-II) with dispersed sphalerite. Sphalerite-I has higher Fe, Mn, Cu, Ge, Cd, Ag, Sn, Sb, and In concentrations compared to sphalerite-II, which has higher As, Hg, and Ba levels. The sphalerite geothermometer analysis indicates a low-temperature (below 200 °C) hydrothermal system, with decreasing  $f\text{S}_2$  and lower Fe and Mn content from sphalerite-I to sphalerite-II. The sphalerites' higher Cd and Ge and lower Mn, In, and Ga concentrations align with CD deposits; this is corroborated by deep learning predictions. Additionally,  $\delta^{34}\text{Sv-CDT}$  values (-10 to +5 ‰) suggest basinal brines and seawater as sulfur sources, and Pb isotope ratios indicate a crustal source for both zones. Therefore, the Gunga Pb-Zn deposit is classified as a CD deposit in a passive margin tectonic environment. Detailed analysis is recommended for commercial Pb-Zn and Ge production. Deep-learning algorithms also identified sphalerite of uncertain origin. Various geochemical techniques and discrimination results align with the geological context, demonstrating that the deep learning model based on sphalerite trace elements can be used for rapid screening of Pb-Zn deposits and associated key metals in mineral exploration.

Supplementary data to this article can be found online at <https://doi.org/10.1016/j.gexplo.2025.107771>.

## CRediT authorship contribution statement

**Muhammad A. Gul:** Writing – review & editing, Writing – original draft, Visualization, Software, Methodology, Investigation, Formal analysis, Data curation, Conceptualization. **Huishan Zhang:** Writing – review & editing, Supervision, Resources, Project administration, Methodology, Investigation, Funding acquisition, Formal analysis, Data curation. **Yu Yang:** Writing – review & editing, Visualization, Validation, Methodology. **Guangli Ren:** Writing – review & editing, Resources. **Chao Sun:** Writing – review & editing, Validation, Supervision, Resources, Methodology. **Xiaojian Zhao:** Writing – review & editing, Resources. **Tahir Bin Yousuf:** Software, Methodology, Data curation. **Ahmed Shah:** Writing – review & editing, Resources, Investigation. **Rizwan Sarwar Awan:** Writing – review & editing, Visualization. **Mohamed Faisal:** Writing – review & editing, Visualization, Validation, Data curation. **Xiaoyong Yang:** Writing – review & editing, Supervision, Resources, Project administration, Funding acquisition.

## Consent to participate

Not applicable.

## Consent to publish

Not applicable.

## Ethical approval

This manuscript has not been published elsewhere in part or in entirety and is not under consideration by another journal. We have read and understood your journal's policies, and we believe that neither the manuscript nor the study violates any of these. We have not submitted our manuscript to a preprint server before submitting it to the Journal of Geochemical Exploration.

## Funding

This study was financially supported by the National Natural Science Foundation of China (42372115, 92055314), Innovation Capability Support Program of Shaanxi Province (2022KJXX-91), Basic Research Program of Natural Science in Shaanxi Province (2023-JC-QN-0281), International Geoscience Program (IGCP-741), and National Key Research and Development Program of China (2021YFC2901802).

## Declaration of competing interest

The authors declare the following financial interests/personal relationships which may be considered as potential competing interests: Huishan Zhang reports financial support was provided by National Natural Science Foundation of China. Huishan Zhang reports financial support was provided by Innovation Capability Support Program of Shaanxi Province. If there are other authors, they declare that they have no known competing financial interests or personal relationships that could have appeared to influence the work reported in this paper.

## Acknowledgments

This study was financially supported by the National Natural Science Foundation of China (42372115, 92055314), Innovation Capability Support Program of Shaanxi Province (2022KJXX-91), Basic Research Program of Natural Science in Shaanxi Province (2023-JC-QN-0281), International Geoscience Program (IGCP-741), and National Key Research and Development Program of China (2021YFC2901802). We are also most grateful to Mei Xia, Ruiping Quan, Shengping Li, Kaiyun Chen, Zhian Bao, and Ningchao Zhou for laboratory assistance. We are also thankful to Bolan Mining Enterprises (BME) for their assistance during fieldwork. Great thanks go to Chief Editor for handling the manuscript. We sincerely thank four anonymous reviewers for their constructive remarks and suggestion that greatly helped to improve the final version of the manuscript.

## Data availability

Not applicable.

## References

- Ahsan, S.N., Qureshi, I.H., 1997. Mineral Resources of Lasbela and Khuzdar Districts, Balochistan, Pakistan. *Geol. Bull. Univ. Peshawar* 30, 41–51.
- Belissoint, R., Muñoz, M., Boiron, M.C., Luais, B., Mathon, O., 2016. Distribution and oxidation state of Ge, Cu and Fe in sphalerite by  $\mu$ -XRF and K-edge  $\mu$ -XANES: insights into Ge incorporation, partitioning and isotopic fractionation. *Geochim. Cosmochim. Acta* 177, 298–314. <https://doi.org/10.1016/j.gca.2016.01.001>.
- Bottrell, S.H., Newton, R.J., 2006. Reconstruction of changes in global sulfur cycling from marine sulfate isotopes. *Earth Sci. Rev.* 75, 59–83. <https://doi.org/10.1016/j.earscirev.2005.10.004>.
- Claypool, G.E., Holser, W.T., Kaplan, I.R., Sakai, H., and Zak, I., 1980, The age curves of sulfur and oxygen isotopes in marine sulfate and their mutual interpretation. (1).
- Cook, N.J., Ciobanu, C.L., Pring, A., Skinner, W., Shimizu, M., Danyushevsky, L., Saini-Eidukat, B., Melcher, F., 2009. Trace and minor elements in sphalerite: a LA-ICPMS study. *Geochim. Cosmochim. Acta* 73, 4761–4791. <https://doi.org/10.1016/j.gca.2009.05.045>.
- Cooke, D.R., Bull, S.W., Large, R.R., McGoldrick, P.J., 2000. The importance of oxidized brines for the formation of Australian Proterozoic stratiform sediment-hosted Pb-Zn (Sedex) deposits. *Econ. Geol.* 95, 1–18.

- Figueroa, M.C., Gregory, D.D., 2017. Isotopic and elemental chemistry of sedimentary pyrite: a combined analytical and statistical approach to a novel planetary biosignature. <https://www.researchgate.net/publication/323585344>.
- Fougerouse, D., Cugeronne, A., Reddy, S.M., Luo, K., Motto-Ros, V., 2023. Nanoscale distribution of Ge in Cu-rich sphalerite. *Geochim. Cosmochim. Acta* 346, 223–230. <https://doi.org/10.1016/j.gca.2023.02.011>.
- Freij, N., Gregory, D.D., Verschelden, R., Côté-Mantha, O., 2023. The use of pyrite chemistry to vector toward gold mineralization, an example from the Drogo Prospect, Nunavut, Canada. *Can. J. Min. Pet.* 61, 909–925. <https://doi.org/10.3749/2200071>.
- Frenzel, M., Hirsch, T., Gutzmer, J., 2016. Gallium, germanium, indium, and other trace and minor elements in sphalerite as a function of deposit type - a meta-analysis. *Ore Geol. Rev.* 76, 52–78. <https://doi.org/10.1016/j.oregeorev.2015.12.017>.
- Frenzel, M., Voudouris, P., Cook, N.J., Ciobanu, C.L., Gilbert, S., Wade, B.P., 2022. Evolution of a hydrothermal ore-forming system recorded by sulfide mineral chemistry: a case study from the Plaka Pb-Zn-Ag Deposit, Lavriion, Greece. *Mineral Deposita* 57, 417–438. <https://doi.org/10.1007/s00126-021-01067-y>.
- Ge, C., Huo, J., Gu, H.O., Wang, F., Sun, H., Li, X., Li, W., Yuan, F., 2021. Tectonic discrimination and application based on convolution neural network and incomplete big data. *J. Geochem. Explor.* 220. <https://doi.org/10.1016/j.gexplo.2020.106662>.
- George, L., Cook, N.J., Cristiana, C., Wade, B.P., 2015. Trace and minor elements in galena: a reconnaissance LA-ICP-MS study. *Am. Mineral.* 100, 548–569. <https://doi.org/10.2138/am-2015-4862>.
- Gregory, D.D., et al., 2019. Distinguishing ore deposit type and barren sedimentary pyrite using laser ablation-inductively coupled plasma-mass spectrometry trace element data and statistical analysis of large data sets. *Econ. Geol.* 114, 771–786. <https://doi.org/10.5382/econgeo.4654>.
- Gul, M.A., et al., 2025. Machine learning-driven classification of Pb [sbn] Zn ore deposits using pyrite trace elements and isotopic signatures: a case study of the Gunga deposit. *J. Geochem. Explor.* 272. <https://doi.org/10.1016/j.gexplo.2025.107693>.
- Hartmann, J., Moosdorf, N., 2012. The new global lithological map database GLiM: a representation of rock properties at the Earth surface. *Geochem. Geophys. Geosyst.* 13. <https://doi.org/10.1029/2012GC004370>.
- Hasterok, D., Halpin, J.A., Collins, A.S., Hand, M., Kreemer, C., Gard, M.G., Glorie, S., 2022. New maps of global geological provinces and tectonic plates. *Earth Sci. Rev.* 231, 104069. <https://doi.org/10.1016/j.earscirev.2022.104069>.
- Hedenquist, J., 2003. Sulfdation state of fluids in active and extinct hydrothermal systems: transitions from porphyry to epithermal environments. <https://www.researchgate.net/publication/272507377>.
- Hoggard, M.J., Czarnota, K., Richards, F.D., Huston, D.L., Jaques, A.L., Ghelichkhan, S., 2020. Global distribution of sediment-hosted metals controlled by craton edge stability. *Nat. Geosci.* 13, 504–510. <https://doi.org/10.1038/s41561-020-0593-2>.
- Höll, R., Kling, M., Schroll, E., 2007. Metallogenesis of germanium-a review. *Ore Geol. Rev.* 30, 145–180. <https://doi.org/10.1016/j.oregeorev.2005.07.034>.
- Husain, V., Khan, H., Germann, K., Zak, K., 2002. Geochemical Investigations of Stratabound Gunga Barite Deposits of Khuzdar (Balochistan). *Resource Geology, Pakistan.* <https://doi.org/10.1111/j.1751-3928.2002.tb00116.x>.
- Huston, D.L., Bastrakov, E., 2024. Germanium, indium, gallium and cadmium in zinc ores: a mineral system approach. *Aust. J. Earth Sci.* <https://doi.org/10.1080/08120099.2024.2423772>.
- Jancovic, S., 1986. The Mineral Assosiation and Genesis of Lead Zinc Barite Deposits of Gunga Khuzdar Balochistan.
- Jankovic, S., 1986. The mineral association and genesis of the lead-zinc barite deposit at Khuzdar District, Balochistan, Pakistan. *Geol. Surv. Pakistan Rec.* 21.
- Jazi, M.A., Karimpour, M.H., Malekzadeh Shafaroudi, A., 2017. Nakhla carbonate-hosted [Formula presented] deposit, Isfahan province, Iran: a geological, mineralogical, geochemical, fluid inclusion, and sulfur isotope study. *Ore Geol. Rev.* 80, 27–47. <https://doi.org/10.1016/j.oregeorev.2016.06.010>.
- Jooshaki, M., Nad, A., Michaux, S., 2021. A systematic review on the application of machine learning in exploiting mineralogical data in mining and mineral industry. *Minerals* 11. <https://doi.org/10.3390/min1108016>.
- Kampschulte, A., Strauss, H., 2004. The sulfur isotopic evolution of Phanerozoic seawater based on the analysis of structurally substituted sulfate in carbonates. *Chem. Geol.* 204, 255–286. <https://doi.org/10.1016/j.chemgeo.2003.11.013>.
- Keith, M., Haase, K.M., Schwarzh-Schampera, U., Klemd, R., Petersen, S., Bach, W., 2014. Effects of temperature, sulfur, and oxygen fugacity on the composition of sphalerite from submarine hydrothermal vents. *Geology* 42, 699–702. <https://doi.org/10.1130/G35655.1>.
- Kelley, K.D., Jennings, S., 2004. A special issue devoted to barite and Zn-Pb-Ag deposits in the Red Dog district, Western Brooks Range, northern Alaska. *Econ. Geol.* <https://doi.org/10.2113/gsecongeo.99.7.1267>.
- Lai, X., Chen, C., Yang, Y., Liu, S., Li, Y., Wang, J., Song, Z., Gu, Y., Chen, X., Huang, X., 2023. Constraints on metallogenetic temperature and mineralization style from reflection color of sphalerite. *Ore Geol. Rev.* 161. <https://doi.org/10.1016/j.oregeorev.2023.105634>.
- Leach, D.L., Sangster, D.F., Kelley, K.D., Large, R.R., Garven, G., Allen, C.R., Gutzmer, J., Walters, S., 2005. *Sediment-Hosted Lead-Zinc Deposits: A Global Perspective: Economic Geology*.
- Li, X.M., Zhang, Y.X., Li, Z.K., Zhao, X.F., Zuo, R.G., Xiao, F., Zheng, Y., 2023a. Discrimination of Pb-Zn deposit types using sphalerite geochemistry: new insights from machine learning algorithm. *Geosci. Front.* 14. <https://doi.org/10.1016/j.jgsf.2023.101580>.
- Li, X.M., Zhang, Y.X., Li, Z.K., Zhao, X.F., Zuo, R.G., Xiao, F., Zheng, Y., 2023b. Discrimination of Pb-Zn deposit types using sphalerite geochemistry: new insights from machine learning algorithm. *Geosci. Front.* 14. <https://doi.org/10.1016/j.jgsf.2023.101580>.
- Li, Y., Lin, Z., 2019. Unsupervised pre-training for natural language generation: a literature review. <https://arxiv.org/abs/1911.06171>.
- Liu, W., Mei, Y., Etschmann, B., Glenn, M., MacRae, C.M., Spinks, S.C., Ryan, C.G., Brugger, J., Paterson, D.J., 2023. Germanium speciation in experimental and natural sphalerite: implications for critical metal enrichment in hydrothermal Zn-Pb ores. *Geochim. Cosmochim. Acta* 342, 198–214. <https://doi.org/10.1016/j.gca.2022.11.031>.
- Machel, H.G., 2001. *Bacterial and thermochemical sulfate reduction in diagenetic settings D old and new insights*.
- Machel, H.G., Krouse, H.R., Sassen, R., 1995. *Products and Distinguishing Criteria of Bacterial and Thermochemical Sulfate Reduction*.
- Mahmoodi, P., Rastad, E., Rajabi, A., Alfonso, P., Canet, C., Peter, J.M., 2021. Genetic model for Jurassic shale-hosted Zn-Pb deposits of the Arak Mining District, Malayer-Esfahan metallogenic belt: insight from sedimentological, textual, and stable isotope characteristics. *Ore Geol. Rev.* 136. <https://doi.org/10.1016/j.oregeorev.2021.104262>.
- Meng, Y.-M., Zhang, X., Huang, X.-W., Hu, R., Bi, X., Meng, S., Zhou, L., Zheng, Y., 2024. A review of the Zn-Pb deposits in Sichuan-Yunnan-Guizhou metallogenic region with emphasis on the enrichment mechanism of Ge, Ga and in. *Ore Geol. Rev.* 164, 105853. <https://doi.org/10.1016/j.oregeorev.2023.105853>.
- Miao, Y., Li, W., Zhou, J., Luo, K., Zhou, Y., Chen, S., Fan, Z., Pan, J., 2023. Geology, geochemistry and genesis of the giant Maoping carbonate-hosted Pb-Zn-(Ag-Ge) deposit in northeastern Yunnan Province, SW China. *Ore Geol. Rev.* 161. <https://doi.org/10.1016/j.oregeorev.2023.105648>.
- Mudd, G.M., Jowitt, S.M., Werner, T.T., 2017. The world's lead-zinc mineral resources: scarcity, data, issues and opportunities. *Ore Geol. Rev.* 80, 1160–1190. <https://doi.org/10.1016/j.oregeorev.2016.08.010>.
- Niu, P.P., Jiang, S.Y., Muñoz, M., 2023. Two-stage enrichment of germanium in the giant Maoping MVT Pb-Zn deposit, southwestern China: constraints from in situ analysis of multicolor sphalerites. *Ore Geol. Rev.* 157. <https://doi.org/10.1016/j.oregeorev.2023.105421>.
- Ohmoto, Hiroshi, 1972. *Systematics of sulfur and carbon isotopes in hydrothermal ore deposits*. *Econ. Geol.* 67 (5), 551–578.
- Parsa, M., 2021. A data augmentation approach to XGboost-based mineral potential mapping: an example of carbonate-hosted Zn-Pb mineral systems of Western Iran. *J. Geochem. Explor.* 228. <https://doi.org/10.1016/j.gexplo.2021.106811>.
- Qin, Y., Kong, H., Liu, B., Jiang, H., Hou, X., Huang, J., 2024. Distinguishing the type of ore-forming fluids in gold deposits using pyrite geochemistry and machine learning. *Nat. Resour. Res.* 33, 107–127. <https://doi.org/10.1007/s11053-023-10282-5>.
- Song, Y., Liu, Y., Hou, Z., Fard, M., Zhang, H., Zhuang, L., 2019. Sediment-hosted Pb-Zn deposits in the Tethyan domain from China to Iran: characteristics, tectonic setting, and ore controls. *Gondwana Res.* 75, 249–281. <https://doi.org/10.1016/J.GR.2019.05.005>.
- Song, Y., Hou, Z., Liu, Y., Zhuang, L., Hu, G., 2023. Mississippi Valley-type Zn-Pb deposits in orogenic thrust belts: ore formation in response to synorogenic crustal transposition or extension. *Mineral. Deposita*. <https://doi.org/10.1007/s00126-023-01185-9>.
- Spry, P.G., Mathur, R.D., Teale, G.S., Godfrey, L.V., 2022. Zinc, sulfur and cadmium isotopes and Zn/Cd ratios as indicators of the origin of the supergiant Broken Hill Pb-Zn-Ag deposit and other Broken Hill-Type deposits, New South Wales, Australia. *Geol. Mag.* 159, 1787–1808. <https://doi.org/10.1017/S0016756822000590>.
- Sun, G.T., Zhou, J.X., 2022. Application of machine learning algorithms to classification of Pb-Zn deposit types using LA-ICP-MS data of sphalerite. *Minerals* 12. <https://doi.org/10.3390/min12101293>.
- Sun, G., Zeng, Q., Zhou, J.X., 2022a. Machine learning coupled with mineral geochemistry reveals the origin of ore deposits. *Ore Geol. Rev.* 142. <https://doi.org/10.1016/j.oregeorev.2022.104753>.
- Sun, G., Zeng, Q., Zhou, J.X., 2022b. Machine learning coupled with mineral geochemistry reveals the origin of ore deposits. *Ore Geol. Rev.* 142. <https://doi.org/10.1016/j.oregeorev.2022.104753>.
- Wang, P., Su, S.G., Wang, G.Z., Dong, Y.Y., Yu, D. lin, 2024. Discrimination of deposit types using magnetite geochemistry based on machine learning. *Ore Geol. Rev.* 170. <https://doi.org/10.1016/j.oregeorev.2024.106107>.
- Wen, H., Zhu, C., Zhang, Y., Cloquet, C., Fan, H., Fu, S., 2016. Zn/Cd ratios and cadmium isotope evidence for the classification of lead-zinc deposits. *Sci. Rep.* 6. <https://doi.org/10.1038/srep25273>.
- Wen, H., Zhu, C., Du, S., Fan, Y., Luo, C., 2020. Gallium (Ga), germanium (Ge), thallium (Tl) and cadmium (Cd) resources in China. *Kexue Tongbao/Chin. Sci. Bull.* 65, 3688–3699. <https://doi.org/10.1360/TB-2020-0267>.
- Wu, T., Huang, Z., Wei, C., Ye, L., Yan, Z., Xiang, Z., Hu, Y., Sui, Z., 2023. LA-ICPMS trace elements and C-O isotopes constrain the origin of the Danaopo Cd-Ge-bearing Zn-Pb deposit, western Hunan, China. *Ore Geol. Rev.* 158. <https://doi.org/10.1016/j.oregeorev.2023.105494>.
- Ye, L., Cook, N.J., Ciobanu, C.L., Yuping, L., Qian, Z., Tiegen, L., Wei, G., Yulong, Y., Danushhevskiy, L., 2011. Trace and minor elements in sphalerite from base metal deposits in South China: a LA-ICPMS study. *Ore Geol. Rev.* <https://doi.org/10.1016/j.oregeorev.2011.03.001>.
- Zaigham, N.A., Mallick, K.A., 2000. Bela ophiolite zone of southern Pakistan: tectonic setting and associated mineral deposits. *Bull. Geol. Soc. Am.* [https://doi.org/10.1130/0016-7606\(2000\)112<478:BOZOSP>2.0.CO;2](https://doi.org/10.1130/0016-7606(2000)112<478:BOZOSP>2.0.CO;2).
- Zartman, R.E., Doe, B.R., 1981. *Plumbotectonics-The Model*.

Zhang, J., Shao, Y., Liu, Z., Chen, K., 2022. Sphalerite as a record of metallogenetic information using multivariate statistical analysis: constraints from trace element geochemistry. *J. Geochem. Explor.* 232. <https://doi.org/10.1016/j.gexplo.2021.106883>.

Zhang, H., Song, Y., Sun, J., Hong, J., Khalil, Y.S., Li, Y., Zhang, H., Wang, Z., 2024. A new discovery of mineralization as subseafloor hydrothermal replacement in the

duddar super-large SEDEX lead-zinc deposit in Pakistan. *J. Earth Sci.* 35, 1075–1078. <https://doi.org/10.1007/s12583-024-2015-7>.

Zhao, H., Shao, Y., Zhang, Y., Cao, G., Zhao, L., Zheng, X., 2023. Big data mining on trace element geochemistry of sphalerite. *J. Geochem. Explor.* 252. <https://doi.org/10.1016/j.gexplo.2023.107254>.